Thermographic analysis of topographically controlled Marangoni–Rayleigh–Bénard convection in a fluid with temperature-dependent properties

Wasim Waris, Marcello Lappa [*]

Department of Mechanical and Aerospace Engineering, University of Strathclyde, James Weir Building, 75 Montrose Street, Glasgow, G1 1XJ, UK

A B S T R A C T

Thermal convection in a shallow layer of liquid with an array of metallic (aluminum) cubic elements evenly spaced along the bottom is investigated experimentally using a thermographic technique. The blocks protrude upwards and, although they are prevented from reaching the free surface, their vertical thickness, horizontal size and overall number can be varied parametrically. This configuration is used with the two-fold intention to produce a kind of obstruction or blockage in the flow and, at the same time, to feed thermal convection with heat directly injected into the fluid at a certain distance from the (hot) floor. It is shown that tuning of the physical topography at the bottom and the difference of temperature between the liquid and the external (gaseous) environment is instrumental in enabling internal feedback control over the spontaneous flow behavior. For a fixed geometry and temperature difference, variations in the emerging pattern can also be produced by changing the thickness of the liquid layer, which indirectly provides evidence for the additional degree of freedom represented by the relative importance of buoyancy and Marangoni effects. Overall, such results suggest a novel possible route to the realization of convective motions with complex (but surprisingly regular) organization, which have been rarely obtained in earlier attempts based on conventional setups.

1. Introduction

Natural, more commonly referred to as "buoyancy or gravitational", convection is a mode of heat transportation whereby fluid motion is induced by the differences in density that are produced as a result of differential heating. When a fluid receives an intake of internal energy, it undergoes thermal expansion and a decrease in density. Accordingly, a circulatory pattern is produced, where relatively hot (lighter) fluid rises, whereas colder (heavier) fluid sinks. This process is very common on Earth's surface where, however, other convective mechanisms can also become dominant if specific conditions are attained. This typically happens if the characteristic depth or length of the considered system is reduced, thereby strongly mitigating buoyancy effects and paving the way to other types of convection that do not rely on density in-homogeneities. A paradigmatic example of these alternate 'routes' or occurrences, widespread just as gravitational convection is, is represented by the so-called Marangoni flow, which emerges as a result of thermally induced gradients of surface tension every time an interface separating two liquids or a liquid and a gas is subjected to a temperature

difference (Seta et al. [1]; Gaponenko et al. [2]; Homma et al. [3]). In many circumstances both types of convection can be developed and interact in a relatively complex way depending on the considered conditions (Schwabe [4]; Shevtsova et al. [5,6]; Shi et al. [7]; Gelfgat [8]).

Moreover, these phenomena affect an uncountable number of natural and technological settings (Colinet et al. [9]; Lappa [10–12]; Kaddeche et al. [13]), and this explains why they are still an area of keen interest, which shows no obvious sign of running out of interest yet. In particular, a vast literature exists for configurations with simplified boundary conditions. These have played a central role in this category of studies owing to the related possibility to determine precisely their evolution as a function of a reduced set of parameters. A classical realization of this modus operandi is the widespread practice of considering shallow layers uniformly heated from below, which correspond to the canonical models of Rayleigh-Bénard (RB) and Marangoni-Bénard (MB) convection (according to whether gradients of density or surface tension are the prevailing force driving fluid flow, respectively, Nepomnyashchy and Simanovskii [14]; Ueno et al. [15]; Schwabe [16]; Lyubimova et al. [17]; Lyubimov et al. [18]; Lappa and Ferialdi [19]; Lappa and Boaro

[20]).

Seminal experimental studies on these subjects are due to Busse and coworkers, who identified a zoo of possible instabilities in RB systems, responsible for a variety of spatial and temporal behaviors (according to the considered fluid and the imposed temperature difference, see, Busse and Whitehead [21,22]; Busse and Clever [23,24]; the interested reader being also referred to the very interesting experiments by Krishnamurti [25–27]; Gollub et al. [28]; Motsay et al. [29]; Croquette et al. [30,31]; Plapp [32]). For the companion case represented by the situation in which the top boundary of the liquid layer is a free surface in contact with a gas, relevant (landmark) experimental works are those by Koschmieder and Switzer [33], Thess and Bestehorn [34], Bestehorn [35], Nitschke and Thess [36], Eckert et al. [37], Schwabe [38] and Dauby and Lebon [39], where emphasis was put on the ability of surface-tension driven convection to select patterns with different fundamental spatial symmetries in different regions of the space of parameters.

Despite the simplistic nature of the examined set-ups, this vast and long-lasting series of efforts have led over the years to the establishment of an elegant and important theoretical sub-field of the more general area of thermal convection [12]. This framework has been fed by the application of a variety of methodological approaches of theoretical, analytical and numerical nature, specifically allowed or facilitated by the aforementioned simplicity of the considered geometrical models and related thermal conditions. More recently, however, a need has emerged for a new line of inquiry considering a departure from such idealized circumstances. Indeed, flat walls with uniform temperature, if they exist in nature or technology, are a special case of configurations with thermal inhomogeneities and non-planar geometry (Lappa [40,41] and Lappa and Inam [42], Weppe et al., [43,44]). Thus, fundamental questions persist regarding the role of these factors in problems of practical interest.

Apart from filling the aforementioned gap, pursuing a more speculative impact of related advances, it may be argued that this alternate line of research may also lead to the identification of exotic states of fluid motion that, for now, remain undefined realizations in the mathematical theory of pattern formation in non-linear systems. As such, they may also contribute to the refinement of already existing theories and/or to the elaboration of completely new ones.

In particular, the present work takes inspiration from the earlier experimental investigation (based on a thermographic technique) by Ismagilov et al. [45]. Their simple and elegant analysis of MB convection (buoyancy effects being negligible in their study) revealed the existence of a non-trivial connection between a physical modulation of the bottom hot wall (implemented as bulges having various polygonal shapes or corrugations developing continuously along a fixed direction) and the symmetry properties of the emerging flow. On varying these features, the latter was found to undergo sudden transitions between different planforms, which were commensurate with the physical topography at the bottom, but were differing in terms of ratio of the intrinsic flow wavelength and length scale of the bulges (this ratio being constrained to remain an integer number).

The motivations at the root of the present work also originate from the earlier numerical analysis by Sakhy et al. [46], who investigated mixed Marangoni-buoyancy convection in a liquid film contained in a cylindrical container with a bottom of flat solid substrate heated from below by a non-uniform heat flux. These authors revealed a fascinating set of stationary patterns varying in terms of cell multiplicity and symmetry depending on the relative importance of buoyant and thermocapillary effects.

This causality has been further explored in later numerical investigations such as those by Lappa et al. [47] and Lappa and Waris [48] where the attention was concentrated on situations where the departure from classical RB or MB modes was caused by bulges (blocks) having a cubic shape mounted on the bottom wall rather than by a spatially varying heat flux at a fixed depth. Moreover, as a distinguishing mark

with respect to Ismagilov et al. [45], much thicker layers of liquid were considered, thereby allowing buoyancy to play a significant role. Interestingly, in these circumstances, solid protuberances have been found to prevent the flows from developing the classical rolls or inverted hexagonal cells typical of RB and MB convection in liquid metals [47] and, similarly, to produce vigorous thermal plumes (thermals) able to interfere with classical surface-tension driven effects in silicone oils [48]. Accordingly, it has been clarified that due to the presence of blocks, the set of possible solutions can be significantly modified, resulting in a zoo of possible behaviors, which seem to escape a possible simple definition or classification in the light of the exiting literature. For practical reasons of for 'simplicity, in the abovementioned studies, a possible classification has been attempted as follows: trivial modes of convection where the surface temperature distribution simply reflects (through a 1:1 correspondence) the ordered arrangement of the underlying hot protuberances, patterns that display a notable degree of analogy with the 'parent' convective mechanisms (classical RB and MB flow) and a third category of flows represented by a kaleidoscope of previously unknown states driven by intrinsic self-organization abilities of the considered system.

The present experimental investigation builds on, but also tries to extend these numerical studies by expanding the set of non-dimensional parameters in terms of values of the Prandtl, Rayleigh and Marangoni numbers. In particular, given the intrinsic nature of the considered problem, a thermographic technique is used to visualize directly the thermally induced fluid currents originating from the top of the considered (disjoint) solid blocks with finite-size and study their influence of the emerging (spatially varying) patterns. Furthermore, different fluid depths are examined in order to change the relative importance of the buoyancy and Marangoni effects for a fixed geometry and temperature difference. Specific insights into the results are obtained using typical tools for the analysis of planform formation in non-linear systems and, accordingly, some effort is provided to interpret them, whenever possible, in the light of existing theories for pattern selection in canonical thermal convection systems.

2. Geometrical model and experimental approach

A sketch of the considered experimental setup is shown in Fig. 1. The physical properties of the related materials are listed in Table 1. The fluid container consists of a square metal plate of aluminum having a size of 10×10 cm and 1 mm thickness, on which solid walls of Perspex (1 cm tick and 2 cm tall) have been mounted along each side, thereby leaving 8×8 cm of internal space to be occupied by the considered liquid (up to a total volume of 1.28×10^{-4} m^3, corresponding to 128 ml, in the absence of obstructions at the bottom).

The blocks are also made of aluminum (same material used for the bottom plate) and are mounted along the bottom wall in such a way to maintain their spacing regular along both the x and z horizontal directions. They are available with different vertical sizes as indicated in Table 2.

A commercial component has been used to produce the required uniform heating at the bottom of the fluid container (see Fig. 2a), that is, a MS-H280-Pro Round ceramic coated Steel Hotplate/Stirrer (by which the heating temperature T_{plate} can be increased up to 280 °C in precise 1 °C increments, other specifications being reported in Table 3). This component relies on a standard PID approach, that is, the departure of the desired temperature from the corresponding imposed value is calculated at any time and a correction is applied accordingly (based on a Proportional, Integral, and Derivative feedback mechanism, hence the acronym).

We wish to recall that the use of infrared data for the analysis of Rayleigh-Marangoni-Bénard (RMB) convection or similar convective systems has already been successfully attempted in the past, leading to useful insights into these phenomena (Cerisier et al. [49,50]; Ismagilov et al. [45]; Chauvet et al. [51]; Wang et al. [52]; Wu et al. [53]; Sobac
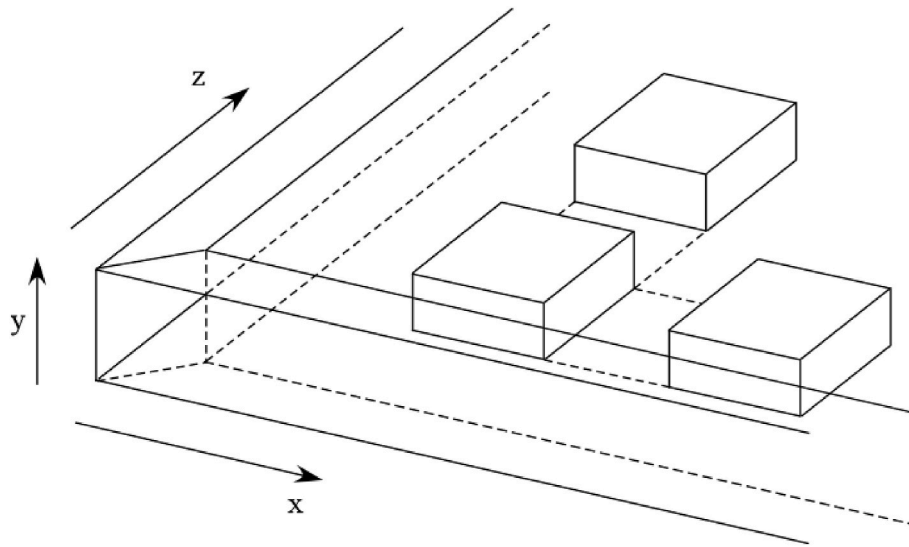
Fig. 1. Three-dimensional view of the fluid container delimited by sidewalls of Perspex with a series of bottom wall-mounted square elements evenly positioned along the sidewall directions (spacing, width and height can be systematically varied).

Table 1
Solid material physical properties (at ambient temperature).

Material	Thermal conductivity (W/mK)	Heat capacity (J/KgK)
Aluminum	240	887
Perspex	0.19	1470

Table 2
Block dimensions.

Horizontal size	Vertical size
10 mm	10 mm
10 mm	5 mm
10 mm	3 mm

et al. [54]; Tönsmann et al. [55]). Here, the distribution of temperature on the free surface of the considered liquid has been obtained using a FLIR C3-X Compact Thermal Imaging Camera (the related IR sensor has a resolution of 128×96 px and thermal sensitivity of 70 mK; moreover, it can detect and measure temperatures between $-20\,°C$ and $+300\,°C$ to an accuracy of $\pm 3\%$). The temperature of the ceramic-coated steel hotplate (as provided by the instrument digital display) and that of the liquid free surface measured by the thermocamera have been verified independently using a 0.3-mm head size K thermocouple connected to an external multimeter (difference $\cong 0.1\,°C$ to be ascribed to the non-negligible size of the thermocouple head).

Additional care has been devoted to confirming the uniformity of the temperature established along the bottom wall of the container sketched in Fig. 1. Using the same thermocouple described above, and after waiting a time of 60 min, in order to allow the overall system to attain steady/stable conditions, the temperature has been measured at different positions along the x and z axes with increments of 1 cm along both directions, thereby leading to a total of more than 60 measurements. The differences among distinct measurements have been found to be smaller than $\cong 0.1\,°C$ for a bottom temperature of $30\,°C$ and $\cong 0.3\,°C$ for a bottom temperature of $50\,°C$ (the reader being also referred to the thermographic image shown in Fig. 2c).

The interested reader may consult Fig. 3 for the relationship between the viscosity of the used fluid (Emkarate RL22H oil) and the temperature. Similar plots for the other physical properties of this liquid (thermal diffusivity, specific heat, density, thermal conductivity, etc.) have been already reported in Waris and Lappa [56] and are not duplicated

here for the sake of brevity (see Fig. 2b–h in that work). Here we limit ourselves to recalling that this oil displays an appreciable sensitivity to temperature. While the variations in terms of density, specific heat, thermal conductivity and thermal diffusivity over a range of 100 K are limited to a 10% percentage (or even smaller) of their initial value, the decrease in terms of viscosity can be much more significant (Fig. 3). In particular, by defining the related Prandtl number as:

$$Pr = \nu/\alpha \tag{1}$$

(where ν and α are the liquid kinematic viscosity and thermal diffusivity, respectively), this characteristic number would decreases from $Pr \cong 520$ for ambient temperature conditions to $Pr \cong 175$ for a temperature $\cong 50\,°C$.

The most remarkable implication of this observation is that, by using a single fluid and increasing its average temperature, a range of situations are covered here, comparable, e.g., to the interval of viscosities considered by Cerisier et al. [50], who used 20 cSt silicone oil with Prandtl number $Pr = 206$ at $25\,°C$, 50 cSt silicone oil with $Pr = 474$ at $25\,°C$, and the more viscous oils employed by Wu et al. [53], their kinematics viscosities and the corresponding Prandtl numbers being $\nu = 1.5, 2, 5, 10,$ and 50 cSt and $Pr = 16.16, 25.21, 62.5, 113.38,$ and 467.29, respectively (we will come back to the implications of this observation later).

As a concluding remark for this section, we wish to highlight that, for all the experiments reported in Sect. 4, the temperature of the environment (air) has been controlled by means of a standard air conditioning system (available in the lab) and kept at a constant value $T_{air} \cong 21 \pm 0.3\,°C$ (as confirmed by independent measurements made using a digital thermometer).

3. Mathematical model and governing parameters

Mapping the experimental problem into a corresponding space of general non-dimensional parameters requires the introduction of additional dimensionless characteristic numbers. For buoyancy and surface-tension driven convection, these can be classically defined as:

$$Ra = g\beta_T \Delta T d^3 / \nu_0 \alpha_0 \tag{2}$$

$$Ma = \sigma_T \Delta T d / \mu_0 \alpha_0 \tag{3}$$

where the first is the canonical Rayleigh number (g and β_T being the
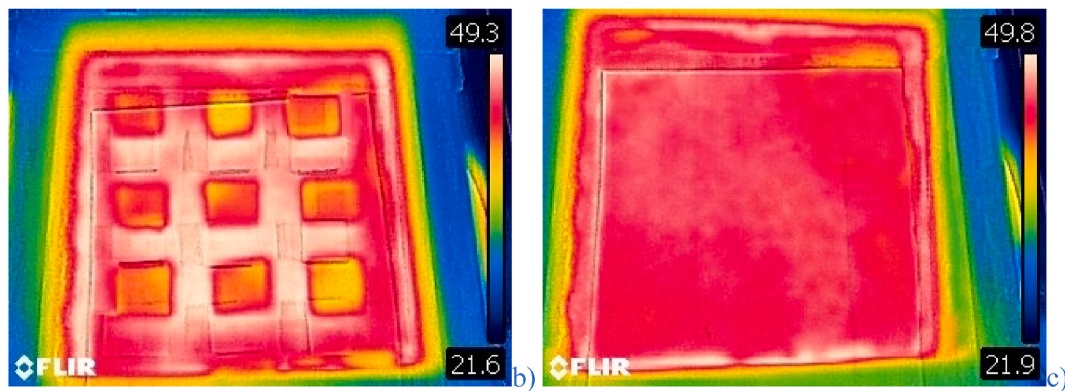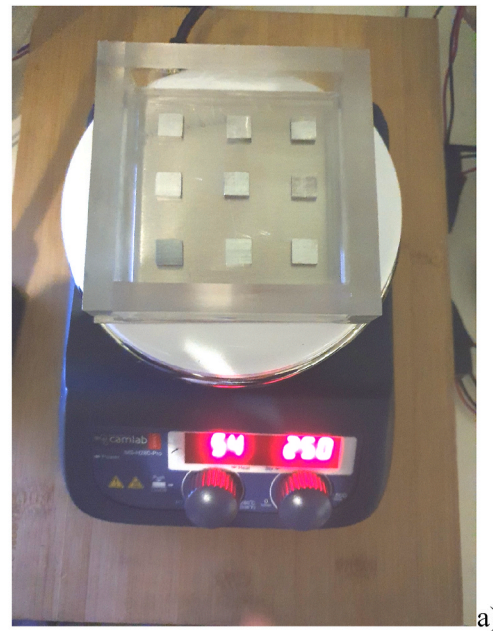
Fig. 2. MS-H280-Pro Round ceramic-coated steel hotplate with diameter 13.5 cm and 10 × 10 cm (diagonal length 14.14 cm) Fluid Container: a) Setup picture (visible light), b) Corresponding thermographic image ($T_{plate} = 50$ °C, no liquid present, i.e. metallic surfaces exposed to air), c) Thermographic image taken in the absence of blocks ($T_{plate} = 50$ °C, no liquid, Note: Metals are known for having high reflectivity, which explains their shiny appearance. This implies a very low emissivity. When a highly polished metal object with a low emissivity is observed with a thermocamera, that surface will act like a mirror. Instead of measuring the temperature of the object itself, the camera will instead detect reflected temperature. In order to fix this issue, the thermographic images of the metal surfaces directly exposed to air reported in this figure have been taken after covering them with a thin layer (0.05 mm) of paper.

Table 3
Specifications of MS-H280-Pro Round ceramic coated Steel Hotplate/Stirrer.

Parameter	Value/range
Work plate Dimension	Φ 135 mm
Work plate material	stainless steel cover with ceramic
Motor type	Brushless DC motor
Motor rating input	5 W
Motor rating output	3 W
Power	515 W
Heating output	500 W
Voltage	100–120/200–240 V 50/60 Hz
Heating temperature range	Room temp.-280, increment 1 °C
Control accuracy of work plate	±1 °C (<100 °C) ±1% (>100 °C)
External temperature sensor	PT1000 (accuracy ±0.5 °C)
Dimension [W × D × H]	150 × 260 × 80 mm
Weight	1.8 kg

gravity acceleration and the thermal expansion coefficient, 9.81 ms^{-2} and $\cong 7.7 \times 10^{-4}$ K^{-1} for the considered liquid, respectively) and the second represents the well-known Marangoni number (σ_T being the

surface tension derivative coefficient, $\cong 0.218$ mNm^{-1} K^{-1} in the present case). In both expressions, d is a characteristic length (the depth of the liquid layer) and, similarly, ΔT accounts for a representative temperature difference, which here is defined as the difference between the temperature of the steel heating plate (T_{plate}) and that of the ambient (T_{air}), i.e. $\Delta T = T_{plate} - T_{air}$ (this temperature difference, much higher than that effective through the liquid, is used here for practical purposes as the temperature of the free liquid-gas interface is not known a priori; moreover, this temperature is expected to behave as a spatially varying quantity in the presence of convection).

For a situation where the physical properties of the fluid can undergo strong variations like in the present case, a 'reference state' must also be defined for the evaluation of the other physical properties appearing in these definitions (namely, μ, ν and α). Here, these are evaluated at $T_0 = T_{air}$ (where, as explained in Sect. 2, $T_{air} \cong 21$ °C).

Besides the three independent parameters Pr, Ma and Ra accounting for the relative importance of various effects (molecular transport of momentum vs heat transport, surface tension or buoyancy versus viscous forces, etc), the problem also depends on its *coupling with the*
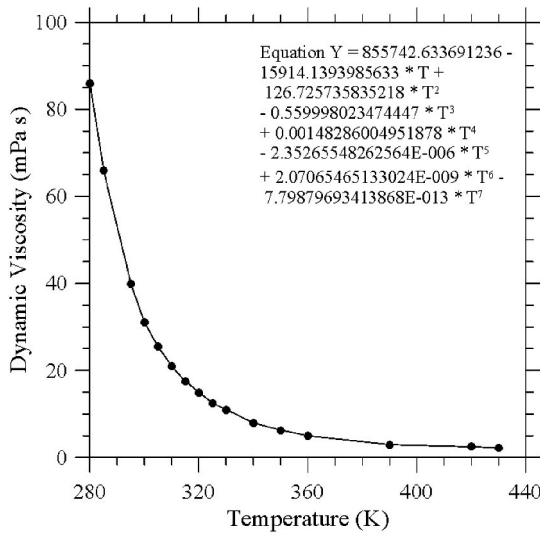
Fig. 3. Dynamic viscosity μ of Emkarate RL22H as a function of temperature as provided by the manufacturer.

external gas. In this regard, it is worth recalling that these systems can develop properties that appear as a consequence of the intrinsic physical mechanisms governing their evolution, and properties that arise as a result of their interaction with the environment (see, e.g., Cerisier et al. [50]; Sakhy et al. [46]). The latter typically depend on the heat exchange effectively occurring at the free surface with the overlying gas.

Although, this observation might be seen as quite an obvious inference, however, an experimental characterization of this effect is not as straightforward as one would imagine. Just like the effective temperature difference established between the heated bottom of the fluid layer and its top cannot be defined 'a priori' (because no thermal control is enforced at the liquid free surface, which therefore attains a temperature essentially depending on the fluid-dynamic phenomena established inside the liquid), in a similar way the heat lost should be considered as a 'derived' quantity, i.e. an outcome of the experiments, rather than an 'input' parameter. For completeness, in the present work, an estimate of such effect is obtained through evaluation of the related (buoyant) convective heat exchange coefficient *h*. In turn, this is determined as a function of the 'observed' (measured) spatially averaged surface temperature T_{surf} (determined electronically by means of Matlab), using the following empirical relationship:

$$h = 0.54 \frac{\lambda_{air}}{L_c} Ra_{air}^{1/4} \tag{4}$$

known to be valid for $10^4 \leq Ra_{air} \leq 10^7$ (see, e.g. Cengel et al., [57]), where $Ra_{air} = \frac{g\beta_{air}(T_{surf}-T_{air})(L_c^3)}{\nu_{air}^2}Pr_{air}$, $L_c = A_{plate}/4L_{plate} = L_{plate}/4$, A_{plate} is the area of the free surface in contact with the external gas and the physical properties of air are evaluated at $T_{airavrg}=(T_{air} + T_{surf})/2$. Accordingly, the surface non-dimensional Biot number (required for problem theoretical closure) is finally computed as:

$$Bi = \frac{hd}{\lambda_{liquid}} \tag{5}$$

with λ_{liquid} being evaluated at $T_{airavrg}$ as well.

Although, as explained before, this should not be regarded as an independent governing (definable a priori) number, it will be used in the following for a more complete characterization of the observed dynamics.

Another meaningful characteristic parameter (it measures the relative importance of buoyancy and Marangoni effects), is the so-called dynamic Bond number, which can be simply introduced as:

$$Bo_{dyn} = Ra/\mathrm{Ma} = \rho g\beta_T d^2/\sigma_T \tag{6}$$

Unlike all the other non-dimensional groups defined before, notably, the direct dependence on the temperature difference is filtered out in this non-dimensional group, which implies that, for a fixed liquid, it essentially scales with the square of the depth of the considered layer. Other relevant 'geometry-scaling' factors required for the characterization of the considered problem are the non-dimensional extensions of the blocks along the directions of the reference system and their aspect ratios A_{xbar} and A_{zbar}:

$$\delta_x = \frac{\ell_x}{d}, \delta_y = \frac{\ell_y}{d}, \delta_z = \frac{\ell_z}{d}, \tag{7a}$$

$$A_{xbar} = \frac{\delta_y}{\delta_x}, A_{zbar} = \frac{\delta_y}{\delta_z} \tag{7b}$$

where ℓ_x, ℓ_y and ℓ_z represent the dimensional size of each element along the three reference directions of the coordinate system shown in Fig. 1.

Similarly, the aspect ratios of the entire fluid domain can be defined as:

$$A_x = \frac{L_x}{d}, A_z = \frac{L_z}{d} \tag{8}$$

where L_x and L_z are the related (dimensional) horizontal lengths ($A_x = A_z = A = L/d$ if $L_x = L_z$). Indicating by N the number of blocks (elements) along z and by M the corresponding number along x, the nondimensional distance between adjoining elements can therefore be expressed as

$$\xi_x = \frac{L_x - M\ell_x}{Md} = \frac{A_x}{M} - \delta_x, \quad \xi_z = \frac{L_z - N\ell_z}{Nd} = \frac{A_z}{N} - \delta_z \tag{9}$$

As in the present work the projections of the entire liquid domain and each element in the xz plane are perfect squares, obviously, the following identities hold: $L_x = L_z$, $\ell_x = \ell_z \rightarrow A_x = A_z$, $A_{xbar} = A_{zbar}$, N = M and $\xi_x = \xi_z$.

4. Results

As already explained to a certain extent in the introduction, the present paper may be regarded as a sequel to two earlier (purely numerical) studies, where the ability of an increasing number of blocks to induce multicellular states with varying degrees of complexity and self-organization was investigated for a fixed aspect ratio of the blocks, fixed values of the Prandtl, Marangoni and Rayleigh numbers and fixed layer thickness. Moreover, the physical properties of the liquid were assumed constant. Here, all these constraints are removed through a four-fold approach relying on a liquid with temperature-dependent physical properties [56], blocks with variable height (as shown in Table 2), increasing values of the temperature of the bottom plate (for a fixed value of the ambient gas temperature) and different liquid depths.

In doing so, we follow a logical process in which one influential factor is varied at a time, while the others are kept fixed. Such a specific hierarchy is obviously instrumental for the selective identification of specific system trends, which would remain otherwise out of reach due to the intertwined nature of many of these dependences. For the convenience of the reader, some of these can be briefly illustrated as follows. While a larger temperature difference contribute to increase directly (through a direct linear proportionality law) both the Marangoni and Rayleigh number by a similar percentage (in such a way that their ratio, i.e. the dynamic Bond number remains constant), an increase in the liquid depth can cause a mismatch or disparity in the ensuing increase of these non-dimensional parameters (which display a linear and cubic dependence on the system size, respectively); accordingly, a significant variation of Bo_{dyn} can be produced.

Also, the block size and aspect ratio have obviously an impact on the possible emerging solutions.

In order to clarify these dynamics, in the following, an extensive parametric analysis is carried out. In particular, the following ranges are investigated: $15 \leq \Delta T \leq 30$ °C, $0.75 \leq d \leq 1.5$ cm and $3 \leq \ell_y \leq 10$ mm (see again Table 2), corresponding to O(1) $\leq Bo_{dyn} \leq$ O(10), $5.3 \leq A \leq 10.6$, $0.3 \leq A_{bar} \leq 1.0$, $0.2 \leq \delta_y \leq 0.66$ in terms of non-dimensional parameters. As already explained in Sect. 2, the temperature field is obtained from the infrared radiation emitted by the oil-gas interface. Moreover, the resulting images are digitized in order to allow the extraction of some relevant (quantitative) data using an appropriate Matlab based software (already extensively used by Waris and Lappa [56] for a posteriori computer-based reconstruction of the spatial distribution of wavelengths in inclined layer convection).

For all the cases reported in the following, the temperature maps shown in the figures have been recorded after a time of 60 min. As this time exceeds the characteristic thermal diffusive time t_d for all the considered conditions ($670 \leq t_d \leq 2700$ s for $0.75 \leq d \leq 1.5$ cm if a representative thermal diffusivity of 8.3×10^{-8} m^2/s is assumed [56]), the duration of each experiment can be considered sufficiently high to allow the system to attain an asymptotic state. The thermographic images have been taken with the camera at a distance of 20 cm from the liquid free surface. For the majority of cases, patterns *with time-independent topological properties have been found* and this has been verified by observing their evolution over other 30 min (leading the total duration of each experiment to at least 1.5 h). Like [48], localized oscillations have occasionally been detected (e.g., for ΔT larger than $\cong 27$ °C and $\cong 21$ °C in the 7.5 mm and 10 mm depth cases, respectively). Although, the threshold for the emergence of these effects is slightly dependent on the presence of blocks, however we have seen only minor variations in terms of patterning behavior (consisting of minor modulations in the shape and size of the thermal spots due to localized 'vibrating' spokes), which explains why in the following we essentially

concentrate on 'spatial' rather than temporal aspects. Notably, all these patterns have been found to be reproducible by repeating the experiment at a different time (on different days).

For the convenience of the reader, we start from the simplest possible situation, that is, the case with a shallow single block located in the center of the domain (a situation formally resembling that investigated numerically by Sakhy et al. [46] for the case of a flat bottom boundary). Moreover, we consider layers with the role of buoyancy increasing as the discussion progresses, that is, we begin the analysis from a layer with thickness 0.75 cm (Sect. 4.1).

4.1. Shallow blocks in shallow layer

Fig. 4 provides a first glimpse of the dynamics observed for the block with height 3 mm located at the bottom of a layer with thickness 0.75 cm ($Bo_{dyn} \cong 1.94$) and increasing values of the temperature set for the bottom hot plate.

It can be seen that for the smallest value of ΔT considered (Fig. 4a), a multicellular configurations is obtained. This is indirectly proven by the distribution of hot spots visible along the free surface, each reflecting the presence of a convective structure with fluid rising (vertically) at the center and descending at the lateral boundary of the cell (after it has exchanged heat with the external environment). Another key observation concerns the number and distribution of such cells. At first glance, indeed, the overall pattern might resemble that typical of classical MB convection. However, upon closer analysis, in qualitative agreement with the numerical findings by Sakhy et al. [46], this figure also reveals that the influence of the central block is not negligible. This is witnessed by the specific arrangement of spots visible in the central part of the domain. While five distinct cells/hot spots can be distinguished along each sidewall, a larger thermal feature occupies the geometrical center of the domain. The hallmark of this specific localized structure is not limited to its (slightly) larger size. Unlike all the other spots, a smaller
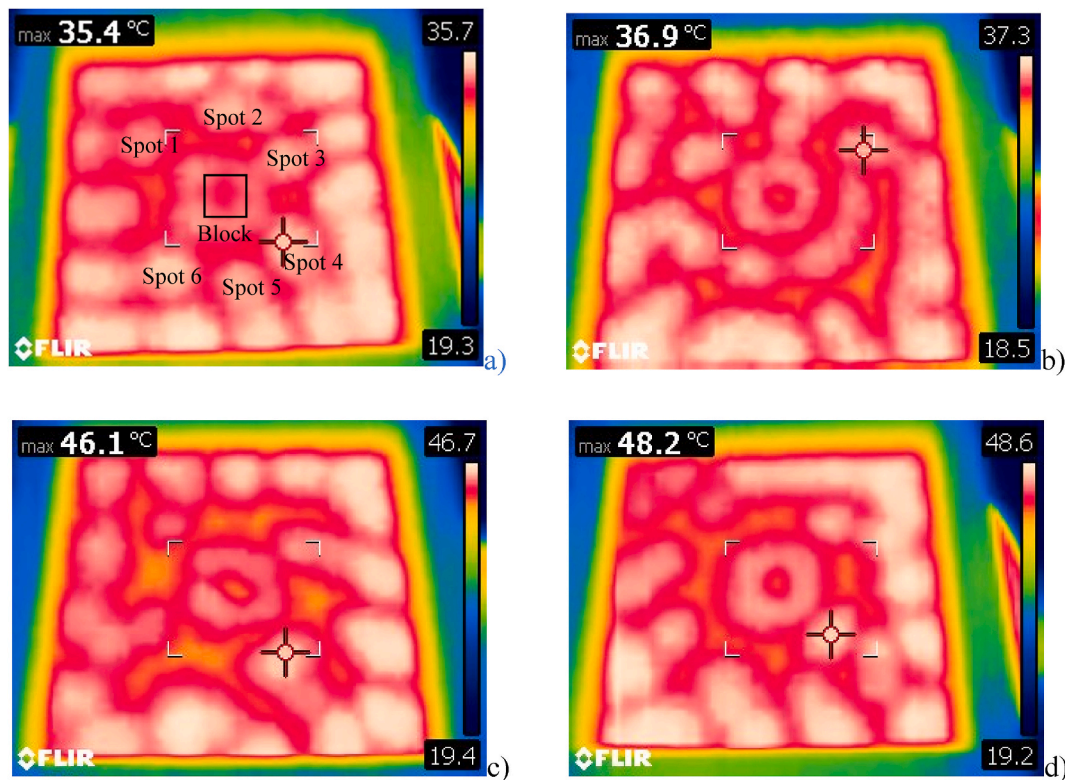

Fig. 4. Depth of the layer 0.75 cm ($A = 10.6$, $Bo_{dyn} \cong 1.94$), N = 1, block thickness 3 mm ($\delta_y = 0.4$, $A_{bar} = 0.3$), variable temperature difference ($Ra \cong 8.6 \times 10^2 \times \Delta T$, $Ma \cong 4.4 \times 10^2 \times \Delta T$): a) $\Delta T = 15$ °C, $Bi \cong 0.347$ (*Note:* the central spot is surrounded by 6 smaller spots), b) $\Delta T = 18$ °C, $Bi \cong 0.358$, c) $\Delta T = 27$ °C, $Bi \cong 0.40$, d) $\Delta T = 30$ °C, $Bi \cong 0.413$. Temperature maps show the descending currents as lines of colder (dark) material.

concentric area is visible. It displays a temperature identical to that of the other regions separating adjoining spots (which, as explained before, correspond to the presence of fluid that after being cooled due to its interaction with the external environment tends to sink), and this leads to the straightforward conclusion that a current of descending fluid is created just above the single block mounted on the bottom (i.e. a toroidal roll is formed just over its top surface, see the sketch in Fig. 5).

Returning to Fig. 4, its next panel (Fig. 4b) indicates that the symmetry of the arrangement of spots in Fig. 4a is lost as the temperature difference is increased. Although the central donut-like thermal feature is maintained, the surrounding pattern undergoes strong modifications. Initially, these consist of spot coalescence phenomena (Fig. 4b), which cause a decrease in the number of spots aligned along the external sidewalls and the formation of an almost circular circuit or 'ring' of spots encapsulating the central thermal feature. On a further increase of the temperature difference, also this specific scheme is lost in favor of a more disordered patterning behavior (Fig. 4c–d).

On increasing N to 2 (Fig. 6), the ability of the topography to influence the pattern strengthens as witnessed by the multiplicity of the thermal features linked to the underlying blocks by a 1:1 correspondence. The thermal inhomogeneities induced at the free surface by the elements at the bottom always manifest as warmer regions with a relatively large spatial extension in comparison to the other minor spots located in proximity to the walls. In turn, the number of these (see, e.g., Fig. 6a) is smaller than that visible in Fig. 4 for N = 1 (3 spots aligned along each sidewall in place of 4).

Overall, for not too high values of ΔT, the pattern for N = 2 obeys the D_4 symmetry group (Lappa and Waris [48]), that is, the set of reflections applicable to a regular polygon with 4 vertices. These include mirroring with respect to the lines perpendicular to the container sidewalls (parallel to the x and z axes shown in Fig. 1), which pass through the geometrical center of the domain and the analogous property with respect to the diagonal directions, i.e. the lines passing through diametrically opposite vertices. As a result, the center of the domain behaves as a special point (knot) with four-fold topology where the fluid (reaching it along four different horizontal directions) is finally pushed towards the bottom of the layer. The chosen disposition of the blocks within the container is compatible with these symmetries, which are retained by the emerging flow. Obviously, this concept cannot be extended to the up-down reflection, which is broken in any case because of the free upper surface and the presence of blocks [48].

Apart from the above-mentioned interesting information about the symmetries which are retained or violated, the major significance of these findings resides in the confirmation they provide about the ability of hot protuberances to behave as 'catalysts', by forcing currents of rising warm fluid to form at fixed positions. These behave as 'pillars', which can somehow 'stabilize' the pattern, i.e. make it much more regular with respect to those which would be produced with no topography. Suffice to recall that in the absence of topography, fluid convection would be characterized by a disordered distribution of rolls with

different orientations and/or convective cells emerging at different positions. Moreover, such a distribution would change on repeating the experiments in identical conditions due to the well-known random initial spatial orientation of the convective structures emerging in both RB and MB convection.

Along the same lines, frame-by-frame comparison of Figs. 6 and 4 also indicates that as N is increased, the transition to a disordered pattern is delayed to larger values of the ΔT, which may be regarded as a further demonstration or verification of the stabilizing role that the bottom hot blocks can have on the emerging behaviors. This realization indeed finds its ultimate verification in the dynamics shown in Fig. 7, yet for a layer with depth 0.75 cm for N = 3.

Regardless of the considered value of ΔT, a total of nine spots with well-defined square shape and highly ordered arrangement can be distinguished in this figure. This means that conditions are attained for which the features of the surface temperature field can be *directly mapped into the topography at the bottom*, i.e. they simply reflect the (a-priori-set) order of the underlying grid of hot blocks (while all the other minor spots are suppressed, a solution hereafter simply referred to as 'saturated state'). However, a closer inspection of these figures also reveals that, although disordered patterns are no longer possible, on increasing the ΔT, the D4 symmetry can still be broken due to some 'localized effects'. These manifest as localized star-shaped figures (Fig. 7b).

4.2. Tall blocks in shallow layer

A replacement of the blocks having thickness 3 mm with the 5 mm ones has a two-fold effect. For N = 1, the central thermal feature that was displaying a donut shape in Fig. 4 (descending flow at the center) is replaced by a full spot (rising fluid at the center, Fig. 8). Moreover, (given the proximity of the top surface of protuberances to the free surface) the size of this central spot is appreciably larger (we argue that due to the limited space between the top surface of the block and the free liquid-gas interface the central toroidal roll described in Sect. 4.1 is no longer formed).

For $\Delta T = 15\,°C$ (Fig. 8a), the ring of spots surrounding the central one displays 8 distinct features in place of the 6 observed in Fig. 4a. For larger ΔT (Fig. 8b), this ordered arrangement is taken over by a relatively disordered distribution of rolls with inclined orientation, which tend to break into separated spots.

The next figure of the sequence (Fig. 9) is instrumental in showing that, moving on to the case with N = 2, a stable pattern preserving the D_4 symmetries is established over the entire interval of temperature differences considered. As a minor difference with respect to the equivalent dynamics depicted in Fig. 6, the aforementioned central 'singular' vertex with four-fold topology (collecting fluid moving horizontally towards it along the free surface, as explained in Sect. 4.1) is taken over by a small spot emerging at the center of the domain.

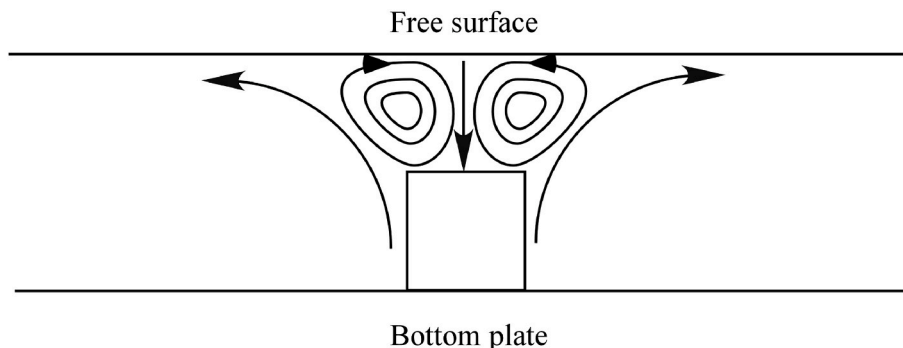Additional insights follow naturally from a comparison of Fig. 9b and

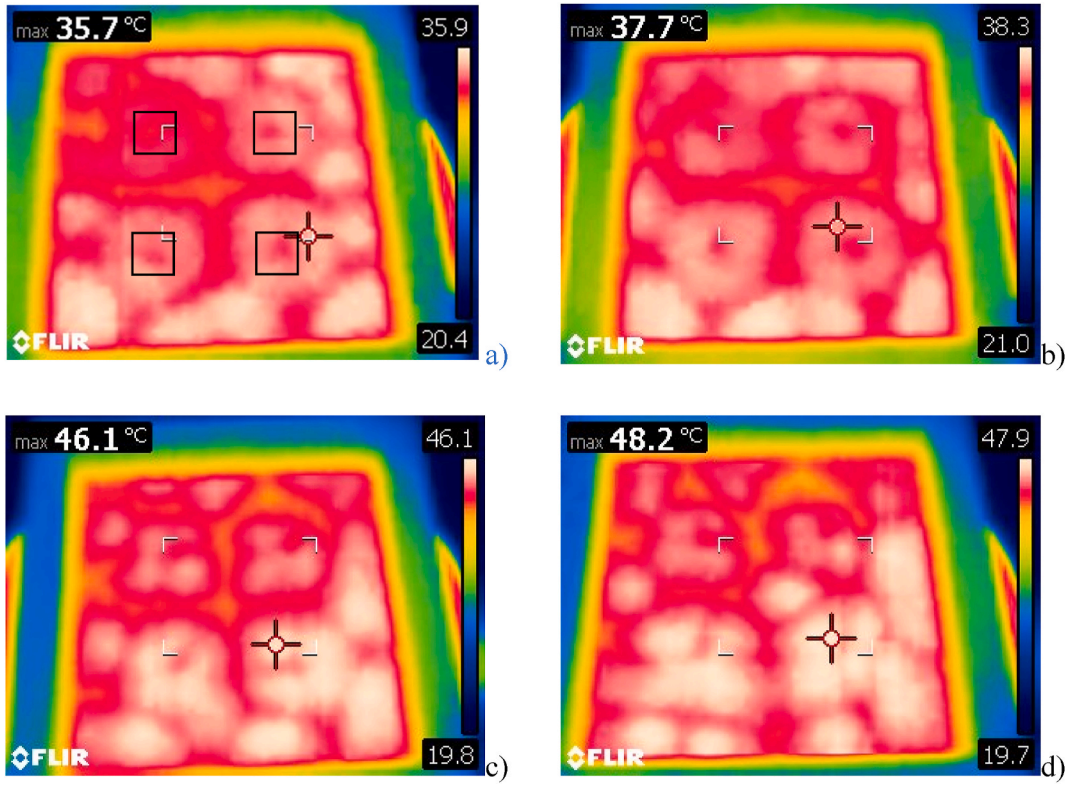**Fig. 5.** Sketch of the toroidal roll formed above the top surface of blocks.

Fig. 6. Depth of the layer 0.75 cm, ($A = 10.6$, $Bo_{dyn} \cong 1.94$), N = 2, block thickness 3 mm ($\delta_y = 0.4$, $A_{bar} = 0.3$), variable temperature difference ($Ra \cong 8.6 \times 10^2 \times \Delta T$, Ma $\cong 4.4 \times 10^2 \times \Delta T$): a) $\Delta T = 15$ °C, $Bi \cong 0.347$ (the black boxes indicate the position of the solid blocks), b) $\Delta T = 18$ °C, $Bi \cong 0.358$, c) $\Delta T = 27$ °C, $Bi \cong 0.40$, d) $\Delta T = 30$ °C, $Bi \cong 0.413$. Temperature maps show the descending currents as lines of colder (dark) material.
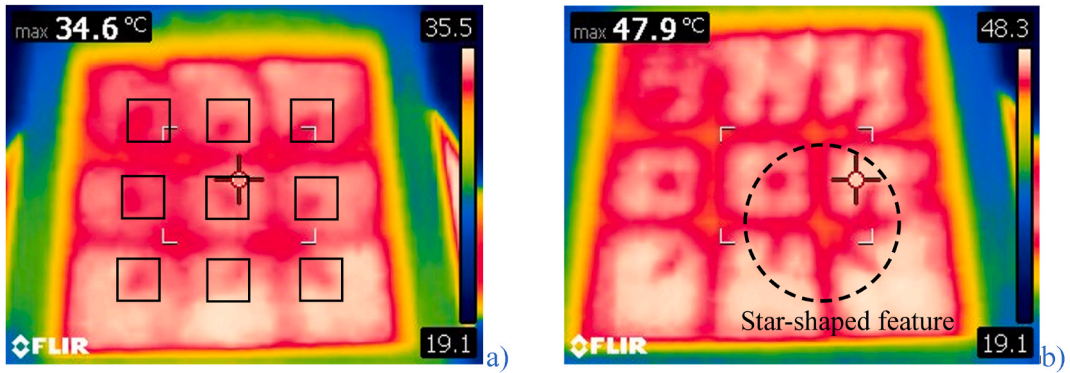
Fig. 7. Depth of the layer 0.75 cm, ($A = 10.6$, $Bo_{dyn} \cong 1.94$), N = 3, block thickness 3 mm ($\delta_y = 0.4$, $A_{bar} = 0.3$), variable ΔT ($Ra \cong 8.6 \times 10^2 \times \Delta T$, Ma $\cong 4.4 \times 10^2 \times \Delta T$): a) $\Delta T = 15$ °C, $Bi \cong 0.347$ (the black boxes indicate the position of the solid blocks), b) $\Delta T = 30$ °C, $Bi \cong 0.413$.

6d. The convective state for a block thickness of 5 mm is much more regular and ordered at the same ΔT, which indicates that for a fixed layer depth the stabilizing role played by the topography strengthens as the thickness of the blocks is increased. The same concept also applies to N = 3 (Fig. 10). The location of spots is simply consistent with the related distribution of protuberances, and an external observer looking at the free surface in this case would naturally be induced to map the set of spots into an array having the same dimensions of the underling matrix of blocks (once again a saturated state condition).

4.3. Shallow blocks in intermediate-depth layer

Having completed a description of the emerging patterns in terms of spatial features for the shallow layer case ($Bo_{dyn} \cong 1.94$), we turn now to considering the companion situations with thicker layer, these

experiments being instrumental in clarifying the nonlinear processes of wavenumber selection at play in these systems. Along these lines, Fig. 11 refers once again to the archetypal N = 1 case. As the reader will realize by inspecting this figure, the most striking difference with respect to the analogous dynamics depicted in Figs. 4 and 8, for relatively small values of the ΔT concerns the size of the emerging thermal features, which increases considerably in the present case (compare e.g., Figs. 11a and 4a). Moreover, for small ΔT the D_4 symmetry is no longer a property of the pattern, this being replaced by a smaller degree of symmetry, namely, the reflectional invariance with respect to a line parallel to the z axis passing through the center of the domain (Fig. 11a). The significance of Fig. 11a and b, however, primarily resides in their ability to make evident that the distribution of wavenumbers is not independent from the ΔT. As the vertical temperature difference grows, the number of convective features becomes higher and accordingly their size shrinks
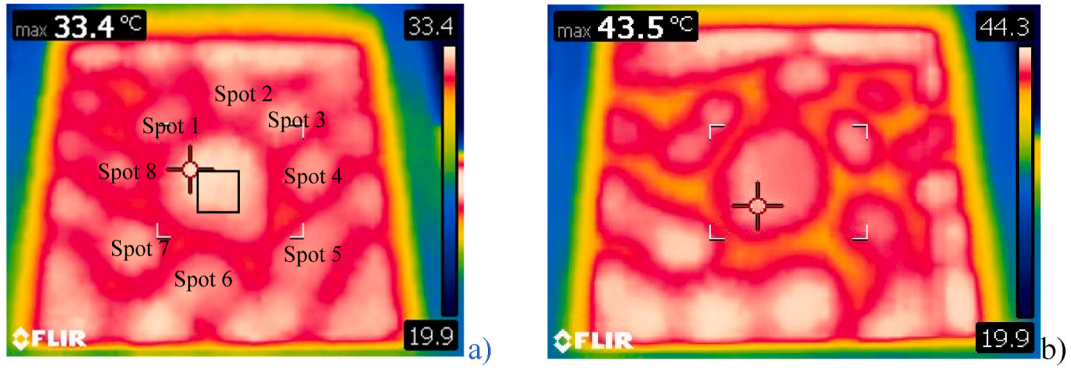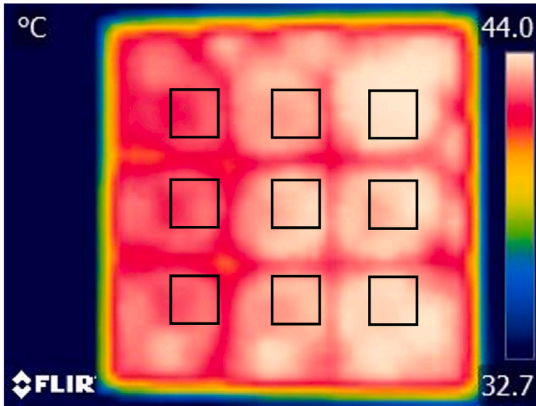
Fig. 8. Depth of the layer 0.75 cm, ($A = 10.6$, $Bo_{dyn} \cong 1.94$), N = 1, block thickness 5 mm ($\delta_y = 0.66$, $A_{bar} = 0.5$), variable temperature difference ($Ra \cong 8.6 \times 10^2 \times \Delta T$, Ma $\cong 4.4 \times 10^2 \times \Delta T$): a) $\Delta T = 15$ °C, $Bi \cong 0.347$ (the black central box indicates the position of the solid block; the central spot is surrounded by 8 smaller spots), b) $\Delta T = 30$ °C, $Bi \cong 0.413$.
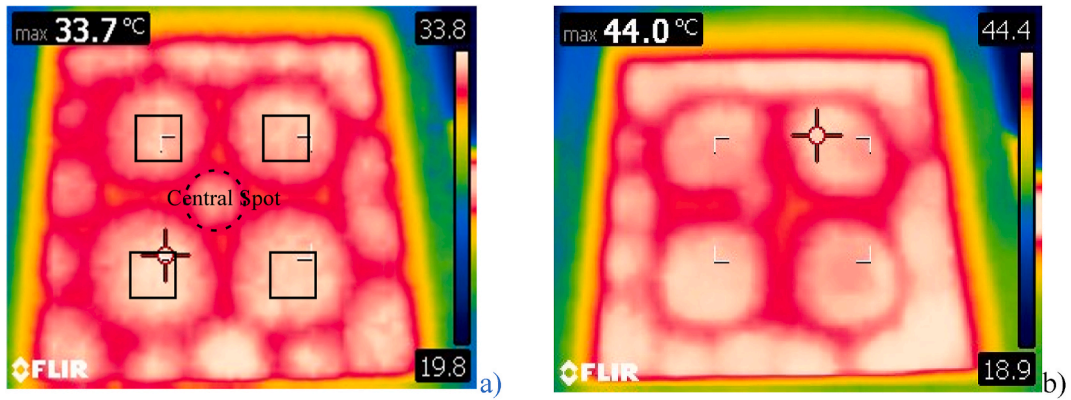
Fig. 9. Depth of the layer 0.75 cm ($A = 10.6$, $Bo_{dyn} \cong 1.94$), N = 2, block thickness 5 mm ($\delta_y = 0.66$, $A_{bar} = 0.5$), variable temperature difference ($Ra \cong 8.6 \times 10^2 \times \Delta T$, Ma $\cong 4.4 \times 10^2 \times \Delta T$): a) $\Delta T = 15$ °C, $Bi \cong 0.347$ (the black boxes indicate the position of the solid blocks), b) $\Delta T = 30$ °C, $Bi \cong 0.413$.

Fig. 10. Depth of the layer 0.75 cm ($A = 10.6$, $Bo_{dyn} \cong 1.94$), N = 3, block thickness 5 mm ($\delta_y = 0.66$, $A_{bar} = 0.5$, the black boxes indicate the position of the solid blocks), $\Delta T = 30$ °C, $Bi \cong 0.413$ ($Ra \cong 8.6 \times 10^2 \times \Delta T$, Ma $\cong 4.4 \times 10^2 \times \Delta T$).

(thereby indicating that an increase in ΔT can cause a rise in the wavenumber, we will come back to this concept later).

For N = 2, the pattern is very ordered (Fig. 12a), with four central spots encapsulated into an external ordered arrangement displaying 3 spots along each side. On increasing the ΔT, however, the symmetry is broken (Fig. 12b). Finally, for N = 3, the trivial aforementioned "saturated state" is recovered over the entire range of ΔT considered (simply reflecting the underlying distribution of elements, not shown).

4.4. Tall blocks in intermediate-depth layer

Following the same approach undertaken in Sect. 4.2, in this section the focus is shifted to the scenario where the vertical size of the blocks is increased while retaining the same layer depth considered in the earlier section (Sect. 4.3). In such a treatment, however, we skip the case N = 1 as the related patterns are almost identical to that already shown in Fig. 11, which leads to the conclusions that for this depth (or value of the dynamic Bond number, i.e. $Bo_{dyn} \cong 3.44$) the ability of a single block to influence the overall pattern is relatively limited.

On considering values of N larger than 1, however, some interesting localized effects become evident (Figs. 13 and 14).

The phenomena originally seen in Fig. 7 for a depth 0.75 cm, N = 3 and block thickness 3 mm also manifest in this case. In particular, as a result of an instability affecting the toroidal roll located above each block (as witnessed by the position of the inner colder spot located at the center of any square hot spot), some special knots appear in the domain, which can be uniquely identified through the topological order p of the radial spokes that emanate from them. For N = 2, notably, one of these special points is located just in the center of the domain (Fig. 13) and its topological order is p = 8. Remarkably, the p = 8 multiplicity is still present for N = 3 (Fig. 14), although the related knots no longer occupy the center of the domain. Owing to this asymmetry, knots with topological order p = 6 are present in addition to the standard one with p = 4 (a similar effect can also be noticed in Fig. 7).

4.5. Shallow blocks in thick layer

This section and the next one (Sect. 4.6) are finally used to describe
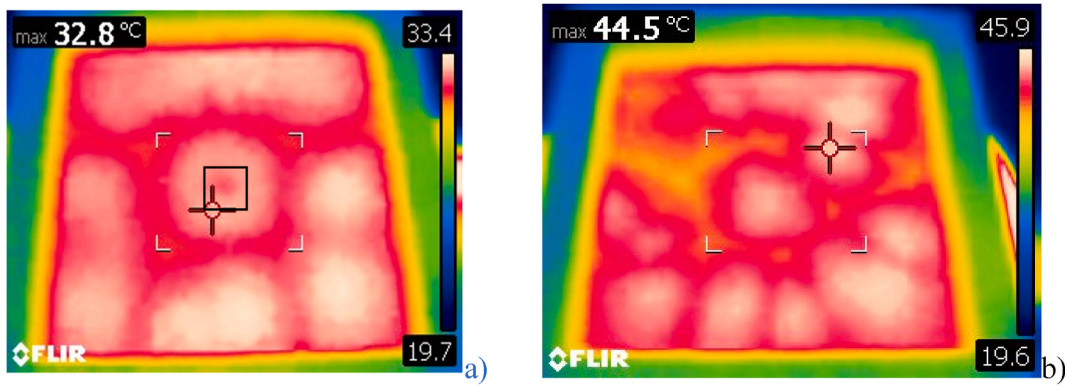
Fig. 11. Depth of the layer 1 cm ($A = 8$, $Bo_{dyn} \cong 3.44$), N = 1, block thickness 3 mm ($\delta_y = 0.3$, $A_{bar} = 0.3$), variable temperature difference ($Ra \cong 2.0 \times 10^3 \times \Delta T$, Ma $\cong 5.9 \times 10^2 \times \Delta T$): a) $\Delta T = 15$ °C, $Bi \cong 0.44$ (the black central box indicates the position of the solid block), b) $\Delta T = 30$ °C, $Bi \cong 0.538$.
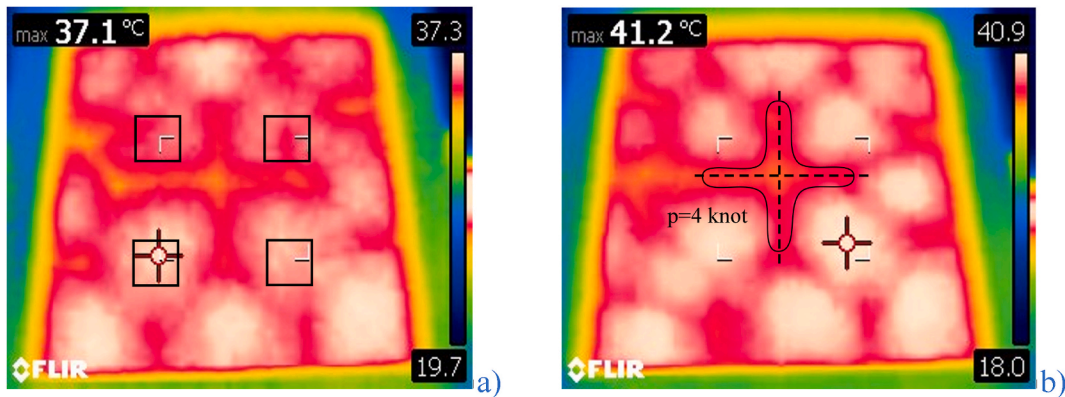
Fig. 12. Depth of the layer 1 cm ($A = 8$, $Bo_{dyn} \cong 3.44$), N = 2, block thickness 3 mm ($\delta_y = 0.3$, $A_{bar} = 0.3$), variable temperature difference ($Ra \cong 2.0 \times 10^3 \times \Delta T$, Ma $\cong 5.9 \times 10^2 \times \Delta T$): a) $\Delta T = 21$ °C, $Bi \cong 0.482$ (the black boxes indicate the position of the solid blocks), b) $\Delta T = 27$ °C, $Bi \cong 0.525$ (topological order of central knot p = 4).
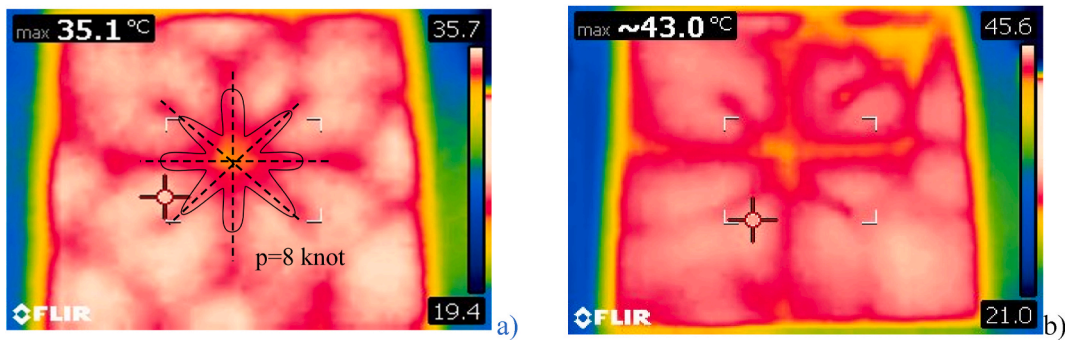
Fig. 13. Depth of the layer 1 cm ($A = 8$, $Bo_{dyn} \cong 3.44$), N = 2, block thickness 5 mm ($\delta_y = 0.5$, $A_{bar} = 0.5$), variable temperature difference ($Ra \cong 2.0 \times 10^3 \times \Delta T$, Ma $\cong 5.9 \times 10^2 \times \Delta T$): a) $\Delta T = 21$ °C, $Bi \cong 0.482$, b) $\Delta T = 30$ °C, $Bi \cong 0.538$ (topological order of central knot p = 8).

the dynamics for a layer with thickness 1.5 cm (doubled with respect to that considered in Sects. 4.1 and 4.2).

In line with the trends highlighted in the earlier sections, by which an increase in the layer depth and/or temperature difference causes a breakdown in the symmetry of the emerging pattern, Fig. 15 clearly shows that for a single block (N = 1) with height 3 mm in a layer with depth 5 times this height, no specific spatial order exists over the entire range of temperature differences considered.

As the ΔT is increased, the wavenumber becomes higher and some "spokes" separating spots having *asymmetric square* or hexagonal shape appear, thereby making the pattern similar to those reported by other authors for the case of pure buoyancy convection (we will come back to

this interesting concept in Sect. 5).

For N = 2 (Fig. 16) a trivial pattern with four large spots is obtained over the entire range of ΔT considered, which indicates that for this layer depth the system enters the saturated state condition for a smaller value of N (compare with Figs. 6 and 12).

4.6. Tall blocks in thick layer

A scenario similar to that described in Sect. 4.5 still holds when the height of the block is increased.

While Figs. 17 and 18 provide a glimpse of the more complex dynamics that are enabled when N = 1 regardless of the thickness of the
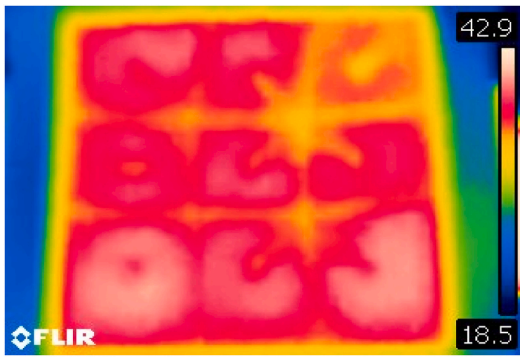
Fig. 14. Depth of the layer 1 cm ($A = 8$, $Bo_{dyn} \cong 3.44$), N = 3, block thickness 5 mm ($\delta_y = 0.5$, $A_{bar} = 0.5$), $\Delta T = 27$ °C, $Bi \cong 0.525$ ($Ra \cong 2.0 \times 10^3 \times \Delta T$, Ma $\cong 5.9 \times 10^2 \times \Delta T$).

considered block (this being 5 mm and 10 mm in Figs. 17 and 18, respectively), a saturated state is recovered as soon as N is increased to 2 or 3 (not shown).

5. Discussion

In order to interpret the present findings, a review of certain results appearing in the literature is beneficial, in particular, a short excursus into the peculiar properties of RB convection in problems that lack the up-down reflection property may help to filter out those aspects which are typical of this form of convection with respect to those induced by the presence of blocks and/or a thermal inhomogeneity at the bottom.

As the reader will have realized at this stage, in the present case, the up-down symmetry is broken due to the contribution of three independent factors, namely, 1) the strong dependence of some fluid properties

on the temperature (as discussed to a certain extent in Sect. 2), 2) the presence of a free surface (as opposed to the no-slip conditions at the bottom) and 3) the existence of hot protuberances along the floor (the topography).

Often hexagonal and asymmetric square convective cells have been observed in the literature even in circumstances where no topography was present in conditions where the first or the second factors were at play, relevant examples being the works by Palm [58] and Golubitsky et al. [59] for the situation with temperature-dependent viscosity and by Demircan and Seehafer [60] for the case of RB convection in layer with a free surface. In this regard it is also worth citing Clever and Busse [61], who found a pattern resembling that shown in Fig. 15d for a fluid layer delimited by solid walls both from above and from below (see F ig. 4.25 in Ref. [12]).

Most interestingly, Demircan and Seehafer [60] demonstrated by means of numerical simulations that, if stress-free conditions are considered at the horizontal boundaries in place of no-slip ones, square patterns appear in RB convection via the Skewed Varicose instability of rolls. In particular, square cells are made possible by the nonlinear interaction of modes with two different wavenumbers that are excited at the same time. These interacting modes can produce bifurcations leading to periodic alternation between a non-equilateral hexagonal pattern and a square pattern or to different kinds of standing oscillations [60]. It is also worth recalling that this oscillatory behavior of dynamical side swapping in square convection can also be found in Marangoni-Bénard convection (see, e.g., Ondarcuhu et al. [62] and Krmpotic et al. [63], where it was still interpreted as the nonlinear interaction between different critical modes).

Re-examination of the present results in the light of this knowledge seems to indicate that, although the propensity to develop square convection is indeed present in some circumstances, however, in general, it should be regarded as the natural tendency of the considered system to develop saturated states when N is increased (the reader being referred
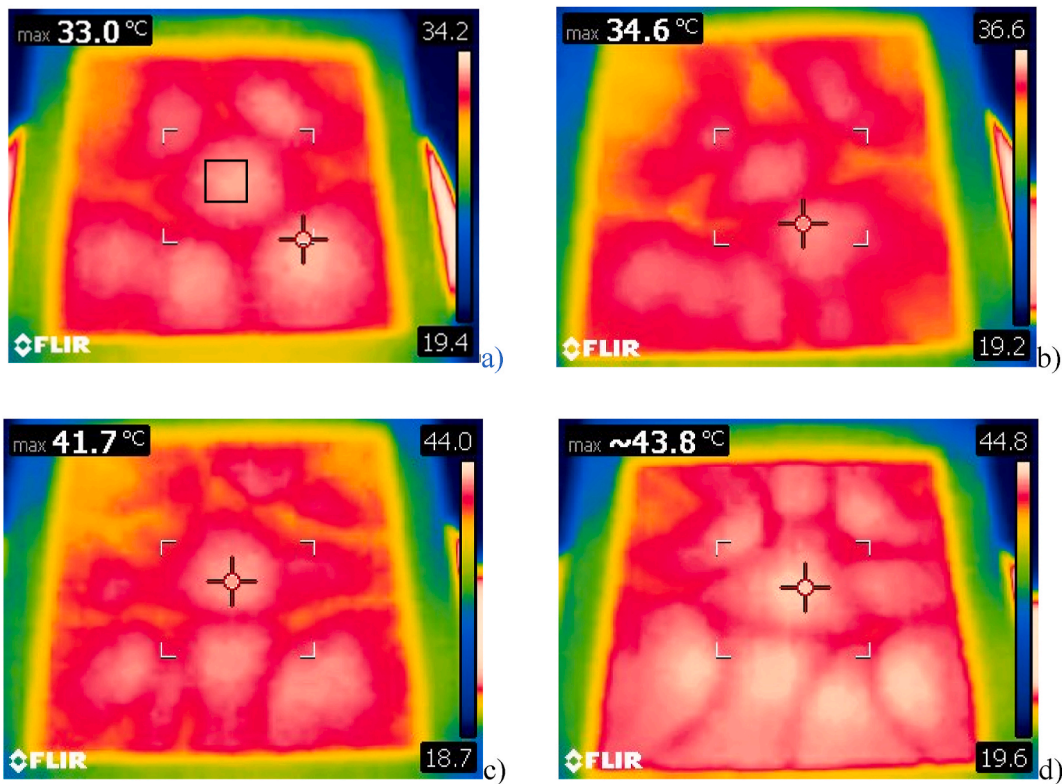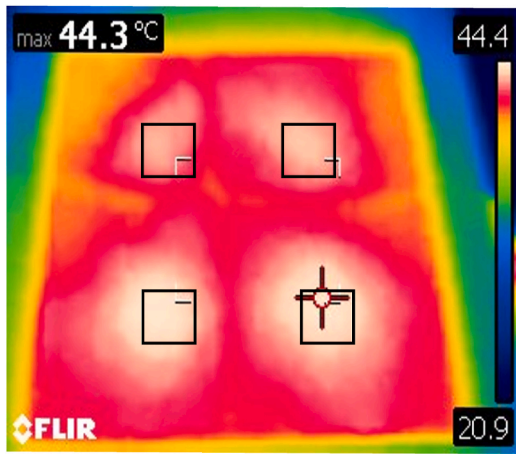

Fig. 15. Depth of the layer 1.5 cm ($A = 5.3$, $Bo_{dyn} \cong 7.75$), N = 1, block thickness 3 mm ($\delta_y = 0.2$, $A_{bar} = 0.3$), variable temperature difference ($Ra \cong 6.85 \times 10^3 \times \Delta T$, Ma $\cong 8.8 \times 10^2 \times \Delta T$): a) $\Delta T = 15$ °C, $Bi \cong 0.65$ (the black central box indicates the position of the solid block), b) $\Delta T = 18$ °C, $Bi \cong 0.673$, c) $\Delta T = 27$ °C, $Bi \cong 0.78$, d) $\Delta T = 30$ °C, $Bi \cong 0.8$.

Fig. 16. Depth of the layer 1.5 cm ($A = 5.3$, $Bo_{dyn} \cong 7.75$), N = 2, block thickness 3 mm ($\delta_y = 0.2$, $A_{bar} = 0.3$, the black boxes indicate the position of the solid blocks), $\Delta T = 30$ °C, $Bi \cong 0.8$ ($Ra \cong 6.85 \times 10^3 \times \Delta T$, Ma $\cong 8.8 \times 10^2 \times \Delta T$).

once again to Figs, 7, 10 and 16). Moreover, the considered cases display the ability to give rise to *more complex states or behaviors*.

As indicated by the present findings, on the one hand, thermals developing in the fluid due to the presence of blocks can dramatically limit the tendency of these systems to produce disordered patterns and multiple solutions, i.e. solutions that coexist in the space of phases and are selected depending on the initial conditions. On the other hand, however, features can be produced, which would not be a solution to the

classical situation with no topography.

In order to clarify this second aspect, in the following, in particular, we consider the case N = 1 for which, as illustrated in Sect. 4, the influence of the topography on the resulting pattern is mediated by the depth of the layer, the height of the block and the temperature difference (i.e. the central block displays a variable degree of success in influencing the overall dynamics depending on d, ℓ_y and ΔT, which provides a hint for the existence of interesting scaling laws).

In particular, the impact of a single block on the distribution of non-dimensional wavelengths (made non-dimensional using the layer depth) is quantitatively substantiated in the three maps obtained for $d = 0.75$, 1 and 1.5 cm, shown in Figs. 19–21 for $Bo_{dyn} \cong$ 1.94, 3.44 and 7.75, respectively.

The wavelength has been obtained as follows: a Matlab based algorithm able to turn any thermographic image provided by the camera into a corresponding "table" of numerical values (i.e. a matrix with a given number of rows and columns) has initially been used to get the set of quantitative data to be used for the ensuing wavelength determination analysis; a second Matlab based algorithm has been exploited to perform a kind of FFT (Fast Fourier Transform) analysis on each row (corresponding to a temperature profile in the x direction) and column (corresponding to a temperature profile along the z direction) pertaining to the considered matrix. An example of this approach can be found in Ref. [48] where it was implemented to extract the spectrum of the surface temperature distribution provided by numerical simulations of Marangoni-Bénard convection for high values of the Marangoni number (see Fig. 5 in that work). Here, for a fixed temperature difference ΔT, for each temperature profile along x or z directions, the "local" wavelength has been obtained as the "period" of the considered temperature profile. More precisely, for each signal (row or column) a discrete set (i.e. a
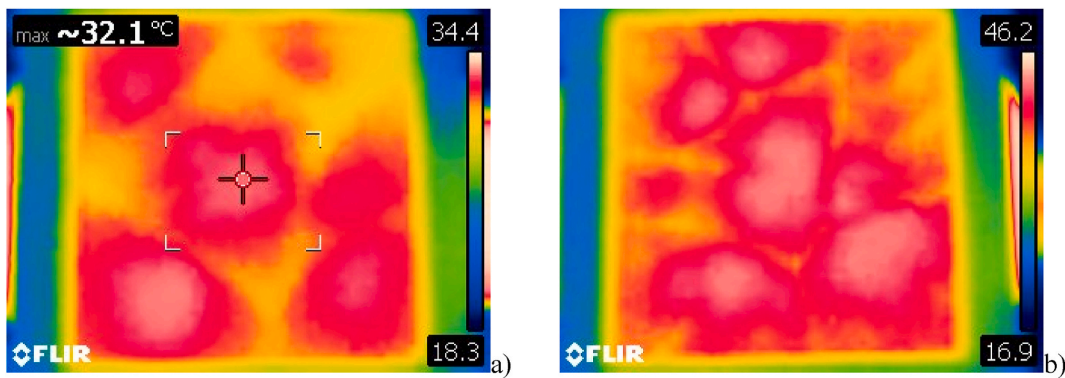
Fig. 17. Depth of the layer 1.5 cm ($A = 5.3$, $Bo_{dyn} \cong 7.75$), N = 1, block thickness 5 mm ($\delta_y = 0.33$, $A_{bar} = 0.5$), variable temperature difference ($Ra \cong 6.85 \times 10^3 \times \Delta T$, Ma $\cong 8.8 \times 10^2 \times \Delta T$): a) $\Delta T = 15$ °C, $Bi \cong 0.65$, b) $\Delta T = 30$ °C, $Bi \cong 0.8$.
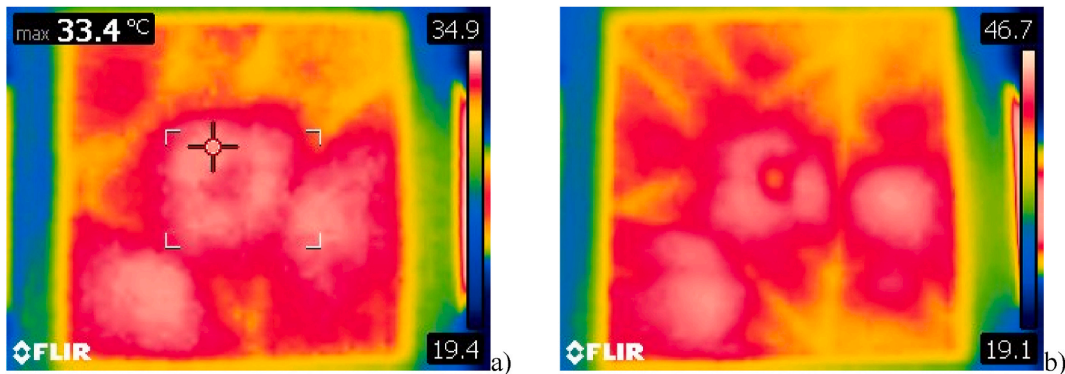
Fig. 18. Depth of the layer 1.5 cm ($A = 5.3$, $Bo_{dyn} \cong 7.75$), N = 1, block thickness 10 mm ($\delta_y = 0.66$, $A_{bar} = 1$), variable temperature difference ($Ra \cong 6.85 \times 10^3 \times \Delta T$, Ma $\cong 8.8 \times 10^2 \times \Delta T$): a) $\Delta T = 15$ °C, $Bi \cong 0.65$, b) $\Delta T = 30$ °C, $Bi \cong 0.8$.
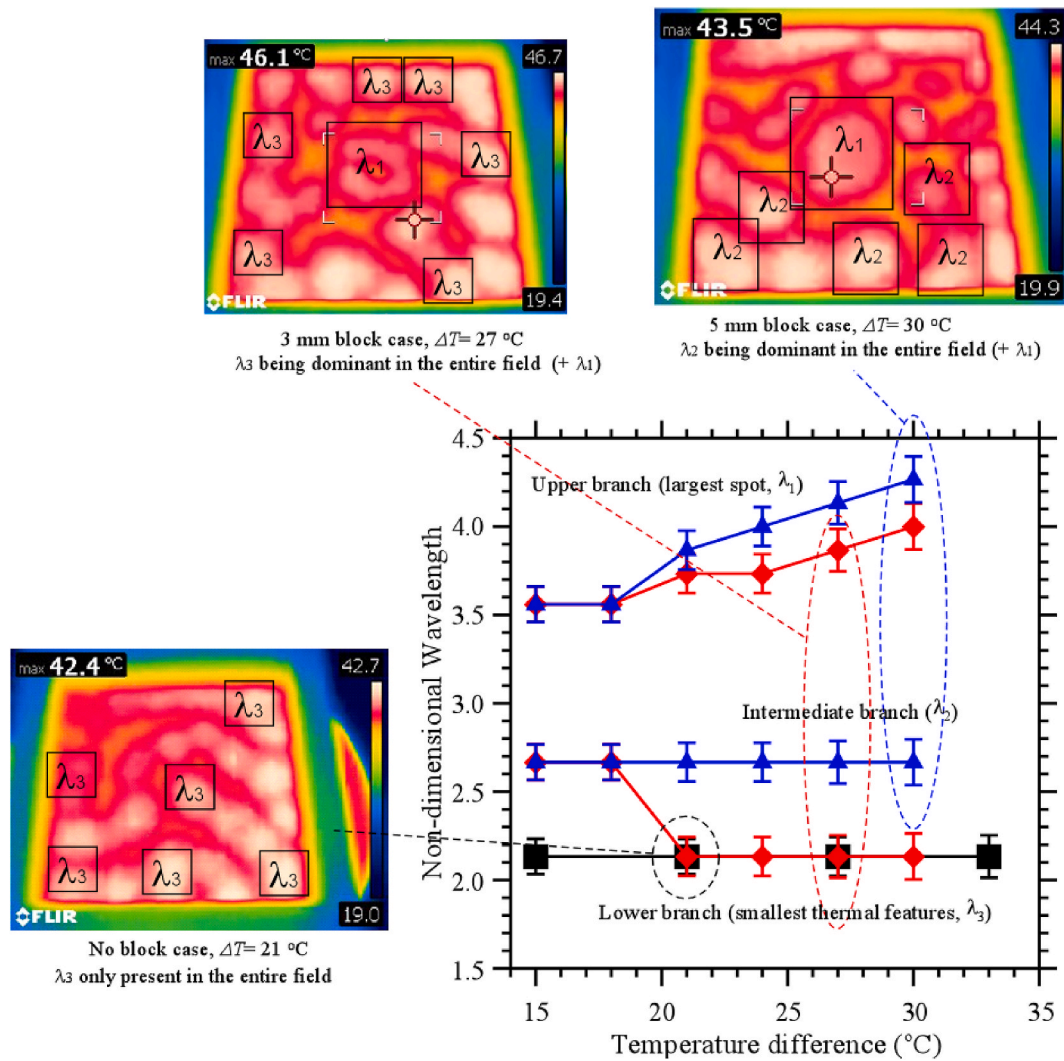
Fig. 19. Wavelength as a function of the temperature difference between the bottom plate and the ambient for the layer with depth 7.5 mm ($Bo_{dyn} \cong 1.94$; Legend: black ■ - No block, red ◆ - 3 mm block, blue ▲ - 5 mm block; the insets are examples used to support reader's understanding of the relationship between the patterning behavior and the related spatial spectrum in terms of wavelengths).

limited number) of wavelengths has been obtained, which represents the (spatial) "spectral" content of the considered temperature (spatial) profile (just like a set of temporal frequencies would represent the spectral content of an oscillatory-in-time signal). This procedure has led to the identification of 2–4 different "characteristic" wavelengths being present in the entire fluid domain for each ΔT over the entire set of columns and rows (hereafter, these wavelength are simply referred to as λ_1, λ_2 and λ_3, with $\lambda_1 > \lambda_2 > \lambda_3$; a fourth relatively small wavelength has been found only in a few cases, only for $\Delta T > 25$ °C). As expected (given the problem symmetries) the recurring wavelengths along x have found to be almost identical to those found for the z direction. This set of data has been further elaborated as follows: each characteristic wavelength has been averaged over the entire set of rows (columns). The 3 dominant spatially averaged wavelengths obtained in this way represent the data summarized in Figs. 19–21 referred to as the lower, intermediate and upper branches, respectively (the lower and the upper representing the most and least extended thermal features, respectively). These wavelengths have been normalized using the depth of the layer. Finally the uncertainty has been determined as the difference between the maximum and minimum wavelength related to a given averaged value.

These figures can be used to reveal the non-trivial correspondence between the topography and the pattern; multiple occurrences of the same symbol for a fixed value of the temperature difference (e.g., along

the vertical direction in Fig. 19) indicate the presence of *coexisting convective structures with different horizontal extension*. For completeness, quantitative data about experiments with the classical unobstructed layer are also included (the reader being referred to the "no block" symbol and the corresponding snapshots presented as insets).

A first key observation stemming from Fig. 19 ($Bo_{dyn} \cong 1.94$) concerns the visible similarities for the layer with and without topography. Such common features (made evident by the overlapping symbols) clearly indicate that these are inherited from the parent forms of convection (the classical RMB problem).

Comparison of the results with and without blocks, however, is also instrumental in showing that an additional branch of wavelengths (representative of another class of convective features) exists for the block-perturbed case (upper branch in Fig. 19). Notably, in general, an increase in the temperature difference results in larger convective structures only if this branch is considered, whereas no significant dependence of the wavelength on the temperature difference can be noticed for the lower branch.

The required explanation for the perfect horizontal orientation of the lower branch can be elaborated in its simplest form on the basis of the argument that the although the aspect ratio of the fluid domain in this case is relatively large ($A = 10.6$), however it is not sufficiently high to allow the considered system to mimic the behavior of an *infinite layer*
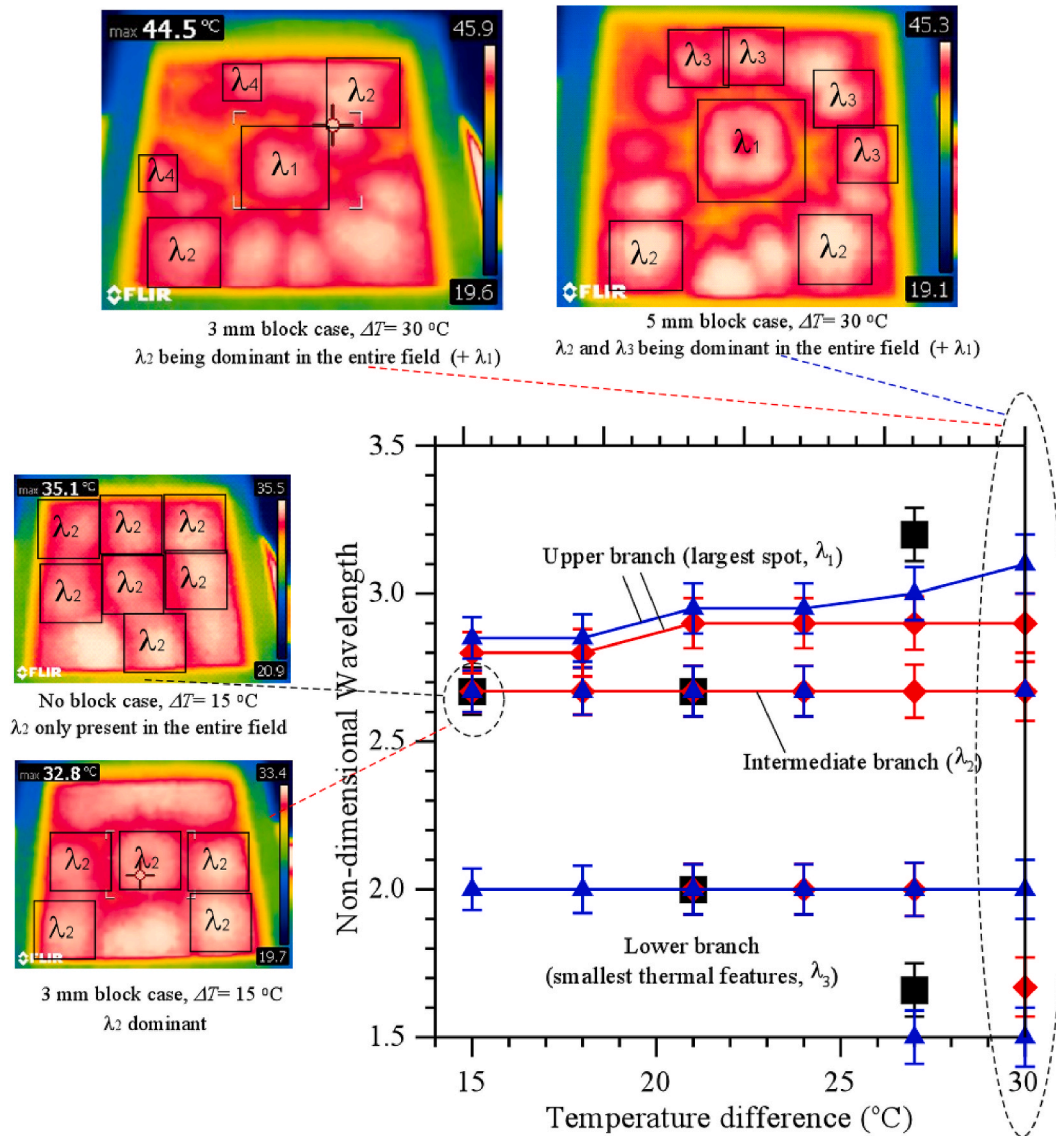
Fig. 20. Wavelength as a function of the temperature difference between the bottom plate and the ambient for the layer with depth 10 mm ($Bo_{dyn} \cong 3.44$; Legend: black ■ - No block, red ◆ - 3 mm block, blue ▲ - 5 mm block; the insets are examples used to support reader's understanding of the relationship between the patterning behavior and the related spatial spectrum in terms of wavelengths).

(which leads to the conclusion that it is prevented from producing continuous changes in the wavelength of the modes of convection pertaining to the parent RMB flow when the imposed ΔT is varied in the considered range; see also Dauby and Lebon [39]).

Interestingly, however, the presence of the block allows the system to develop an 'intermediate' branch of wavelengths, which does not exist in the case with no topography. The use of different colors in this figure is also instrumental in revealing that a net distinction exists between the wavelength for blocks with 3 and 5 mm (upper branch). This implies that the anisotropy introduced by the central block, not only leads to the emergence of a new branch of localized states, but it also cause some readjustments in the general ability of the system to produce other localized convective features (thereby providing a justification for the different extension of the intermediate branch for different vertical sizes of the block).

However, when the depth of the layer is increased to 1 cm (Fig. 20, $Bo_{dyn} \cong 3.44$), it can be seen that the results obtained for blocks having a height of 5 mm and 3 mm are relatively close one another. Moreover, the (vertical) distance of the upper branch (accounting for the presence of the central convective structure) from the other branches becomes

smaller. On a separate note, it is also worth highlighting that, on increasing the ΔT, the central spot displays a tendency to grow whereas the structures produced by standard RMB convection become smaller for $\Delta T \geq 27$ °C (the shrinkage being even more evident for the 5 mm block case).

As the layer depth is increased to 1.5 cm (Fig. 21, $Bo_{dyn} \cong 7.75$), the branch related to the convective cell/spot above the single central block is no longer present. The ability of the block to influence the overall flow is relatively limited as also witnessed by the overlap of wavelengths obtained for the cases 3 mm and 5 mm. Relatively small structures appear only for $\Delta T \geq 27$ °C and in the case with block thickness 5 mm (see the triangle symbols at the very bottom of this figure).

As already discussed to a certain extent in Sect. 4, this variety of coexisting wavelengths tends to be mitigated as N is increased, until the convective features generated by the blocks become so dominant that they prevent the system from adapting to changes in the depth of the layer and/or height of the blocks. In those cases, the system enter the aforementioned "saturated" condition, which explains why figures equivalent to Figs. 19–21 are not being shown here for N = 2 and N = 3.

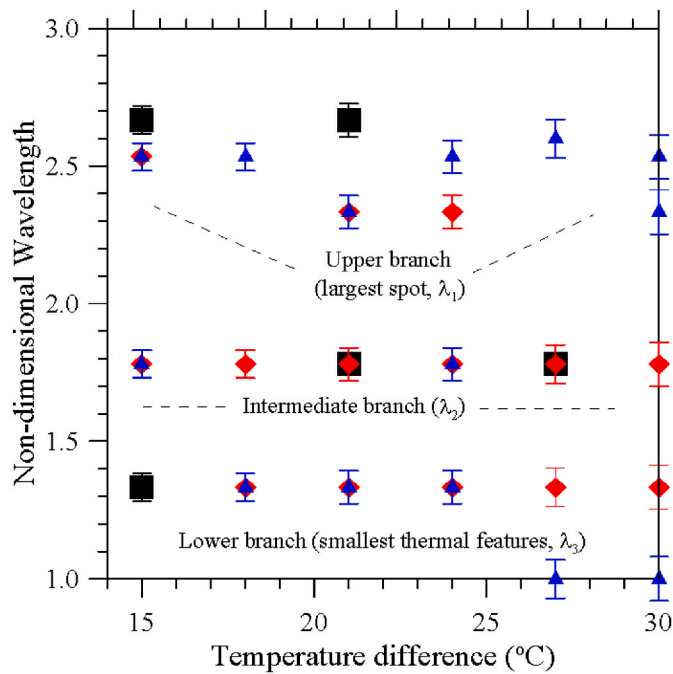Additional insights finally stem from comparison of the present

Fig. 21. Wavelength as a function of the temperature difference between the bottom plate and the ambient for the layer with depth 15 mm ($Bo_{dyn} \cong 7.75$; Legend: black ■ - No block, red ◆ - 3 mm block, blue ▲ - 5 mm block).

experimental findings with the numerical ones by Lappa and Waris [48]. Although those numerical results were obtained for a much smaller value of the Prandtl number and constant viscosity (Pr = 10, as larger values of this parameter would have otherwise required prohibitive computational times), some interesting qualitative considerations can be made. It can indeed be inferred that a fluid with variable (temperature-dependent) physical properties tendentially promotes the emergence of self-organized states such as those shown in Figs. 6, 9, 12 and 13 for smaller values of the parameter N.

6. Conclusions

Complex patterns typical of canonical forms of convection such as MB and RB arise spontaneously as a result of the amplification (and ensuing saturation) of certain categories of disturbances, which are selected out of the full spectrum of possible perturbations because of the symmetry that they satisfy and the isotropy and/or multidirectional translational invariance of the system where they are amplified. Nevertheless, as revealed by the present study, somehow 'engineered' states can be produced through the introduction of a given topography in the system. This can help to meet the desired objective through a two-fold influential process, namely, first (passive control) by limiting the accessibility of the flow to certain regions of the physical domain (breaking the in-plane isotropy of the fluid layer), second (active control) through the buoyancy-induced generation of thermals, which, by acting as 'pillars' can force the pattern to develop nodes with relatively high topological order at fixed points, just like atoms positioned at lattice points in a crystal.

The system response to a change in the topography (N) is mediated by a number of factors, including, the depth of the layer, the height of blocks, the temperature difference and the layer aspect ratio. By following a structured modus operandi aimed to unravel some specific interwoven aspects, we have shown that for N = 1, features of the abovementioned classical forms of convection can still be clearly identified. For small and intermediate depths of the layer, these features correspond to the branches visible in the lower part of the figures (maps) providing the distribution of wavelength as a function of the

temperature difference. In turn, the horizontal orientation of such branches indicates that, for the conditions considered in the present work, i.e. A = O (10), the layer is not sufficiently extended in the horizontal direction to allow a continuous variation of the wavelength with ΔT (in other words, the size of the emerging convective structures represented by these branches is dictated essentially by the aspect ratio of the layer).

The anisotropy introduced by the blocks leads to the emergence of another branch and some related re-adjustments in the other branches. The related ability of the wavelength to scale with the ΔT may be regarded as evidence of the different nature of this convective feature, which is not constrained to obey the rules of standard RMB convection and represents a clear departure from convection in isotropic layers (it clearly draws from fluid motion originating from the hot vertical walls of the block, which allows it to escape the abovementioned rules).

On increasing the layer depth, as expected, the pattern-forming mechanism is transferred back to the parent forms of convection. Remarkably, however, an increase in N has the opposite effect, i.e., the system gradually evolves towards topography-controlled solutions, whereas the properties of the parent forms of convection tend to be suppressed in favor of more system specific ones.

For all the conditions considered in the present work, indeed, the convective features induced by the blocks become dominant with respect to those of the parent RMB convection as soon as N is increased from 1 to 2, regardless of the depth of the layer. These consist of a unique arrangement of square thermal features supporting knots with topological order in the range between p = 4 and p = 8. As already explained before, these are made possible by the thermal plumes generated above the blocks, which act as pillars stabilizing the flow and reducing dramatically the set of allowed wavelengths until a single possible wavelength corresponding to $L/3$, i.e. a trivial state is obtained for N = 3 over a wide range of conditions.

A tendency opposing the emergence of such saturated states is represented by the ability of the planform to develop localized features, which can increase locally the topological order of certain knots and cause a breakdown in its symmetry, especially if relatively small values of the dynamic Bond number are considered. Vice versa, an increase in this parameter can promote asymmetry and disordered patterns in the case N = 1.

In order to expand this line of inquiry, future experiments could be conducted for the situation where the considered multi-block system is inclined with respect to the horizontal direction, thereby opening the door to the ability of gravity-induced shear flow to cause a further breakage (this time at a "global" level) in the in-plane isotropy of the fluid domain.

Declaration of competing interest

The authors declare that they have no known competing financial interests or personal relationships that could have appeared to influence the work reported in this paper.

Data availability

Data will be made available on request.

References

[1] B. Seta, D. Dubert, M. Prats, Jna Gavalda, J. Massons, M.M. Bou-Ali, X. Ruiz, V. Shevtsova, Transitions between nonlinear regimes in melting and liquid bridges in microgravity, Int. J. Heat Mass Tran. 193 (2022) 122984.

[2] Y. Gaponenko, T. Yano, K. Nishino, S. Matsumoto, V. Shevtsova, Pattern selection for convective flow in a liquid bridge subjected to remote thermal action, Phys. Fluids 34 (9) (2022), 092102.

[3] T. Homma, T. Yamashita, R. Wada, T. Tsukahara, I. Ueno, Multicellular structures in thin free liquid films induced by thermocapillary effect, J. Colloid Interface Sci. 641 (2023) 187–196.

[4] D. Schwabe, Buoyant-thermocapillary and pure thermocapillary convective instabilities in Czochralski systems, J. Cryst. Growth 237–239 (2002) 1849–1853.

[5] V.M. Shevtsova, A.A. Nepomnyashchy, J.C. Legros, Thermocapillary-buoyancy convection in a shallow cavity heated from the side, Phys. Rev. E 67 (14) (2003), 066308.

[6] V. Shevtsova, D.E. Melnikov, A. Nepomnyashchy, New flow regimes generated by mode coupling in buoyant-thermocapillary convection, Phys. Rev. Lett. 102 (2009), 134503.

[7] W. Shi, G. Li, X. Liu, L. Peng, N. Imaishi, Thermocapillary convection and Buoyant-thermocapillary convection in the annular pools of silicon melt and silicone oil, J. Supercond. Nov. Magnetism 23 (6) (2010) 1169–1172.

[8] A. Gelfgat, Effect of interface dynamic deformations on instabilities of buoyancy-thermocapillary convection in a two-fluid two-layer system, Phys. Rev. Fluids 7 (5) (2022), 053503.

[9] P. Colinet, J.C. Legros, M.G. Velarde, Nonlinear Dynamics of Surface-Tension-Driven Instabilities, John Wiley, 2001.

[10] M. Lappa, On the nature and structure of possible three-dimensional steady flows in closed and open parallelepipedic and cubical containers under different heating conditions and driving forces, Fluid Dynam. Mater. Process. 1 (1) (2005) 1–19, https://doi.org/10.3970/fdmp.2005.001.001.

[11] M. Lappa, Thermal convection and related instabilities in models of crystal growth from the melt on earth and in microgravity: past history and current status, Cryst. Res. Technol. 40 (6) (2005) 531–549, https://doi.org/10.1002/crat.200410381.

[12] M. Lappa, Thermal Convection: Patterns, Evolution and Stability, John Wiley & Sons, Ltd, Chichester, England, 2009.

[13] S. Kaddeche, J.P. Garandet, D. Henry, H.B. Hadid, A. Mojtabi, On the effect of natural convection on solute segregation in the horizontal Bridgman configuration: convergence of a theoretical model with numerical and experimental data, J. Cryst. Growth 409 (2015) 89–94.

[14] A. Nepomnyashchy, I. Simanovskii, Oscillatory convection instabilities in systems with an interface, Int. J. Multiphas. Flow 21 (1995) 129–139.

[15] I. Ueno, T. Kurosawa, H. Kawamura, Thermocapillary convection in thin liquid layer with temperature gradient inclined to free surface, IHTC12, Grenoble, France 18-23 Aug, 2002.

[16] D. Schwabe, Convective instabilities in complex systems with partly free surface, J. Phys. Conf. 64 (1) (2007), 012001.

[17] T. Lyubimova, D.V. Lyubimov, Ya Parshakova, Implications of the Marangoni effect on the onset of Rayleigh–Bénard convection in a two-layer system with a deformable interface, Eur. Phys. J. Spec. Top. 224 (2015) 249–259.

[18] D.V. Lyubimov, T.P. Lyubimova, N.I. Lobov, J.I.D. Alexander, Rayleigh–Bénard–Marangoni convection in a weakly non-Boussinesq fluid layer with a deformable surface, Phys. Fluids 30 (2018), 024103.

[19] M. Lappa, H. Ferialdi, Multiple solutions, oscillons and strange attractors in ThermoViscoElastic Marangoni convection, Phys. Fluids 30 (10) (2018), 104104, 19 pages.

[20] M. Lappa, A. Boaro, Rayleigh-Bénard convection in viscoelastic liquid bridges, J. Fluid Mech. 904 (2020) 10, https://doi.org/10.1017/jfm.2020.608. December 2020, A2.

[21] F.H. Busse, J.A. Whitehead, Instabilities of convection rolls in a high Prandtl number fluid, J. Fluid Mech. 47 (1971) 305–320.

[22] F.H. Busse, J.A. Whitehead, Oscillatory and collective instabilities in large Prandtl number convection, J. Fluid Mech. 66 (1974) 67–79.

[23] F.H. Busse, R.M. Clever, Instabilities of convection rolls in a fluid of moderate Prandtl number, J. Fluid Mech. 91 (1979) 319–335.

[24] F.H. Busse, R.M. Clever, Asymmetric squares as an attracting set in Rayleigh-Bénard convection, Phys. Rev. Lett. 81 (1998) 341–344.

[25] R. Krishnamurti, On the Transition to Turbulent Convection: Part 1, the transition from two- to three-dimensional flow, J. Fluid Mech. 42 (1970) 295–307.

[26] R. Krishnamurti, On the Transition to Turbulent Convection: Part 2, the transition to time-dependent flow, J. Fluid Mech. 42 (1970) 309–320.

[27] R. Krishnamurti, Some further studies on the transition to turbulent convection, J. Fluid Mech. 60 (1973) 285–303.

[28] J.P. Gollub, A.R. Mccarriar, J.F. Steinman, Convective pattern evolution and secondary instabilities, J. Fluid Mech. 125 (1982) 259–281.

[29] R.W. Motsay, K.E. Anderson, R.P. Behringer, The onset of convection and turbulence in rectangular layers of normal liquid ^{4}He, J. Fluid Mech. 189 (1988) 263–286.

[30] V. Croquette, P. Le Gal, A. Pocheau, Spatial features of the transition to chaos in an extended system, Phys. Scripta T13 (1986) 135–138.

[31] V. Croquette, Convective pattern dynamics al low Prandtl number: Part II, Contemp. Phys. 30 (3) (1989) 153–171.

[32] B.B. Plapp, Spiral Pattern Formation in Rayleigh-Bénard Convection, Ph.D. Thesis, Cornell University, Ithaca, NY, 1997.

[33] E.L. Koschmieder, D.W. Switzer, The wavenumbers of supercritical surface-tension-driven Bénard convection, J. Fluid Mech. 240 (1992) 533–548.

[34] A. Thess, M. Bestehorn, Planform selection in Bénard-Marangoni convection: l hexagons versus g hexagons, Phys. Rev. E 52 (1995) 6358–6367.

[35] M. Bestehorn, Square patterns in Bénard-Marangoni convection, Phys. Rev. Lett. 76 (1996) 46–49.

[36] K. Nitschke, A. Thess, Secondary instability in surface-tension-driven Bénard convection, Phys. Rev. 52 (1995) 5772–5775.

[37] K. Eckert, M. Bestehorn, A. Thess, Square cells in surface-tension-driven Bénard convection: experiments and theory, J. Fluid Mech. 356 (1998) 155–197.

[38] D. Schwabe, The Bénard-Marangoni-instability in small circular containers under microgravity: experimental results, Adv. Space Res. 24 (10) (1999) 1347–1356.

[39] P.C. Dauby, G. Lebon, Bénard-Marangoni instability in rigid rectangular containers, J. Fluid Mech. 329 (1996) 25–64.

[40] M. Lappa, On the oscillatory hydrodynamic modes in liquid metal layers with an obstruction located on the bottom, Int. J. Therm. Sci. 118 (2017) 303–319.

[41] M. Lappa, On the gravitational suppression of hydrothermal modes in liquid layers with a blockage on the bottom wall, Int. J. Therm. Sci. 145 (2019). , 105987.

[42] M. Lappa, S. Inam, Thermogravitational and hybrid convection in an obstructed compact cavity, Int. J. Therm. Sci. 156 (2020) 21, 106478.

[43] A. Weppe, F. Moreau, D. Saury, Experimental study of a natural convection flow in a cubic enclosure with a partially heated inner block, J. Phys.: Conf. Ser. 2116 (2021), 012033.

[44] A. Weppe, F. Moreau, D. Saury, Experimental investigation of a turbulent natural convection flow in a cubic cavity with an inner obstacle partially heated, Int. J. Heat Mass Tran. 194 (2022), 123052.

[45] R.F. Ismagilov, D. Rosmarin, D.H. Gracias, A.D. Stroock, G.M. Whitesides, Competition of intrinsic and topographically imposed patterns in Bénard–Marangoni convection, Appl. Phys. Lett. 79 (3) (2001) 439–441.

[46] R.E. Sakhy, K.E. Omari, Y.L. Guer, S. Blancher, Rayleigh-Benard-Marangoni convection in an open cylindrical container heated by a non-uniform flux, Int. J. Therm. Sci. 86 (2014) 198–209.

[47] M. Lappa, A. Sayar, W. Waris, Topographically controlled Marangoni-Rayleigh-Bénard convection in liquid metals, Fluids 6 (12) (2021) 23, 447.

[48] M. Lappa, W. Waris, On the role of heat source location and multiplicity in topographically controlled Marangoni-Rayleigh-Bénard convection, J. Fluid Mech. 939 (2022) 39. A20.

[49] P. Cerisier, J. Pantaloni, G. Finiels, R. Amalric, Thermovision applied to Benard-Marangoni convection, Appl. Opt. 21 (1982) 2153–2159.

[50] P. Cerisier, S. Rahal, H. Azuma, Pattern dynamics of the Bénard-Marangoni instability in a medium aspect ratio container, J. Phys.: Conf. Ser. 64 (2007), 012004.

[51] F. Chauvet, S. Dehaeck, P. Colinet, Threshold of Bénard-Marangoni instability in drying liquid films. EPL -, Europhys. Lett. 99 (3) (2012), 34001.

[52] J.M. Wang, G.H. Liu, Y.L. Fang, W.K. Li, Marangoni effect in nonequilibrium multiphase system of material processing, Rev. Chem. Eng. 32 (5) (2016) 551–585.

[53] D. Wu, L. Duan, Q. Kang, Wavenumber selection by Bénard–Marangoni convection at high supercritical number, Chin. Phys. Lett. 34 (5) (2017), 054702 (4 pages).

[54] B. Sobac, P. Colinet, L. Pauchard, Influence of Bénard–Marangoni instability on the morphology of drying colloidal films, Soft Matter 15 (2019) 2381–2390.

[55] M. Tönsmann, P. Scharfer, W. Schabel, Critical solutal Marangoni number correlation for short-scale convective instabilities in drying poly(vinyl acetate)-Methanol thin films, Polymers 13 (26) (2021) 2955.

[56] W. Waris, M. Lappa, Patterning behavior of hybrid buoyancy-Marangoni Convection in inclined layers heated from below, Fluids 8 (1) (2023) 12 (30 pages).

[57] Y.A. Cengel, R.H. Turner, J.M. Cimbala, Fundamentals of Thermal-Fluid Sciences, fifth ed., McGraw Hill, 2016.

[58] E. Palm, On the tendency towards hexagonal cells in steady convection, J. Fluid Mech. 8 (1960) 183–192.

[59] M. Golubitsky, J.W. Swift, E. Knobloch, Symmetries and Pattern selection in Rayleigh-Benard convection, Phys. D 10 (1984) 249–276.

[60] A. Demircan, N. Seehafer, Nonlinear square patterns in Rayleigh-Bénard convection, Europhys. Lett. 53 (2) (2001) 202–208.

[61] R.M. Clever, F.H. Busse, Hexagonal convection cells under conditions of vertical symmetry, Phys. Rev. E 53 (1996) R2037–R2040.

[62] T. Ondarcuhu, G.B. Mindlin, H.L. Mancini, C. Pérez García, Dynamical patterns in Bénard-Marangoni convection in a square container, Phys. Rev. Lett. 70 (1993) 3892–3895.

[63] D. Krmpotic, G.B. Mindlin, C. Pérez-García, Bénard-Marangoni convection in square containers, Phys. Rev. E E. 54 (4) (1996) 3609–3613.